

# UniE2F: A Unified Diffusion Framework for Event-to-Frame Reconstruction with Video Foundation Models

Gang Xu<sup>1, 2†</sup>, Zhiyu Zhu<sup>1, 3†</sup>, Junhui Hou<sup>1\*</sup>

<sup>1</sup>Department of Computer Science, City University of Hong Kong, Hong Kong, China.

<sup>2</sup>Guangdong Laboratory of Artificial Intelligence and Digital Economy (SZ), Shenzhen, China.

<sup>3</sup>Department of Computer Science, City University of Hong Kong (Dongguan), Dongguan, China.

\*Corresponding author(s). E-mail(s): [jh.hou@cityu.edu.hk](mailto:jh.hou@cityu.edu.hk);  
Contributing authors: [xugang@gml.ac.cn](mailto:xugang@gml.ac.cn); [zhiyu.zhu@cityu-dg.edu.cn](mailto:zhiyu.zhu@cityu-dg.edu.cn);

†Equal Contribution

## Abstract

Event cameras excel at high-speed, low-power, and high-dynamic-range scene perception. However, as they fundamentally record only relative intensity changes rather than absolute intensity, the resulting data streams suffer from a significant loss of spatial information and static texture details. In this paper, we address this limitation by leveraging the generative prior of a pre-trained video diffusion model to reconstruct high-fidelity video frames from sparse event data. Specifically, we first establish a baseline model by directly applying event data as a condition to synthesize videos. Then, based on the physical correlation between the event stream and video frames, we further introduce the event-based inter-frame residual guidance to enhance the accuracy of video frame reconstruction. Furthermore, we extend our method to video frame interpolation and prediction in a zero-shot manner by modulating the reverse diffusion sampling process, thereby creating a unified event-to-frame reconstruction framework. Experimental results on real-world and synthetic datasets demonstrate that our method significantly outperforms previous approaches both quantitatively and qualitatively. We also refer the reviewers to the **video demo** contained in the *supplementary material* for video results. The code will be publicly available at <https://github.com/CS-GangXu/UniE2F>.

**Keywords:** Event-based Vision; Video Reconstruction; Diffusion Model; Video Foundation Models

## 1 Introduction

Event cameras, also known as dynamic vision sensors, measure high-frequency changes in pixel intensity as “events” and output a continuous flow encoding the time, location, and polarity of each change [1, 2]. This asynchronous processing allows them to capture high dynamic range

scenes (up to 140 dB) with exceptional temporal resolution (approx. 1  $\mu$ s) and low power consumption (5 mW) without motion blur [3, 4]. Building on these advantages, event data has been widely adopted in object tracking [5, 6], semantic segmentation [7], and gaze estimation [8]. While these attributes make event cameras ideal for high frame

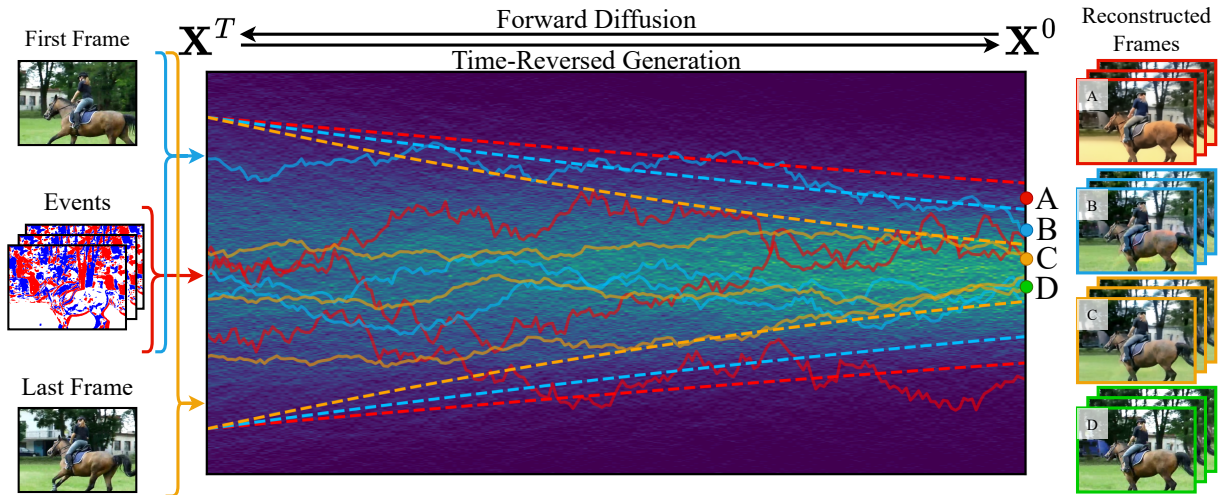


**Fig. 1:** Illustration of the forward and backward diffusion processes for our UniE2F under the conditional event data. The right and left parts indicate the inputs and results of our algorithm, while in the central plot, the solid and dashed lines with the same color represent the reverse-time sampling SDE and ODE trajectories under the same setting, respectively. The proposed method can adapt to different types of event-assisted frame reconstruction tasks. (A) **event-based frame reconstruction:** with input of only event, to reconstruct RGB frame; (B) **frame prediction:** with input of both event and the first frame to reconstruct the remaining frames; and (C) **frame interpolation:** with input of event and the first and last frames to reconstruct the intermediate frames. (D) denotes the ground-truth frames corresponding to the conditional event data.

rate video reconstruction [9, 10], the data is inherently sparse as it only captures relative brightness changes. Consequently, this limited information content has led previous event-based video frame reconstruction approaches [9, 11–14] to reconstruct images that differ *significantly* from the richly detailed scenes observed in real-world environments. Moreover, the current utility of event cameras extends beyond image reconstruction. Their microsecond-level resolution unlocks critical applications in temporal modeling, i.e., video frame interpolation (VFI) [15] and video frame prediction (VFP) [16]. Where standard cameras struggle with high-speed motion, often suffering from blur and temporal gaps, event-based VFI [17, 18] bridges these discontinuities by leveraging continuous event streams to synthesize intermediate frames. This enables applications ranging from smooth slow-motion smartphone photography to latency-critical tasks in autonomous navigation. Similarly, VFP [19, 20] utilizes event dynamics to forecast future states, compensating for hardware limitations in scientific observation. However, due

to the limited model capability, previous work usually processes those tasks of reconstruction, VFI, and VFP have been treated as isolated tasks.

Recently, the diffusion model [21] has shown remarkable progress in image generation and image restoration [22–27], relying on a core mechanism of iterative noise addition and removal to generate realistic outcomes. Through large-scale pre-training, the stable diffusion model [28] has accumulated rich generative prior knowledge and a powerful capability to approximate diverse and complicated distributions. With the aid of conditional information, such as text or image prompts, the stable diffusion model [28] can achieve a more accurate generation process, thereby enhancing the fidelity of details and semantic consistency of the generated content. Furthermore, the stable video diffusion (SVD) model [29], benefiting from large-scale pre-training on video data, also demonstrates its capabilities to produce videos that are both realistic and visually pleasing based on text and image conditions.

In this paper, building on the powerful generative capacity of the SVD model, we propose the

**Unified Framework for Event2Frame (UniE2F)**, which leverages event data as the conditional input to guide the reconstruction process, bridging the gap between sparse event data and highly detailed real-world scenarios. After fine-tuning the SVD model, we introduce the event-based inter-frame residual guidance, which exploits event data to effectively constrain the residual between consecutive reconstructed frames. Specifically, during the reverse diffusion process, this mechanism first predicts the inter-frame residuals from event data. Then, it iteratively refines the intermediate latent via the gradient descent algorithm based on the inter-frame residuals to improve the reconstruction accuracy. In addition to reconstructing video frames purely from the event data, we further adapt the proposed method to event-based video frame interpolation [17, 30–32] and prediction [19] in a *zero-shot* manner.

Based on the powerful generative capacity of mapping sparse and asynchronous event data to continuous video frames, the prior information from the first and last frames for interpolation, or solely from the first frame for prediction, is utilized to guide the reverse diffusion process. Specifically, we modulate the score function by incorporating deviation derived from the discrepancies between the estimated clean latent and the given reference latent, guiding the reverse sampling process to reconstruct intermediate or subsequent frames with enhanced temporal consistency and visual fidelity. As shown in Fig. 1, as more prior information is provided, our UniE2F can produce frames that more closely match the ground truth. Through these designs, we construct a unified event-to-frame reconstruction framework that effectively handles diverse applications while reducing the need for task-specific models. Experimental results on real-world and synthetic datasets demonstrate that our method significantly outperforms previous approaches in both qualitative and quantitative assessments.

In summary, the main contributions of this work are as follows.

- We propose a diffusion-based event-to-frame reconstruction framework that utilizes the event-based inter-frame residual guidance to align the physical correlations between those frames, thus boosting the performance.

- We give a theoretical analysis that optimizing the proposed regularization-based event physical mechanism can indeed help minimize the error upper boundary.
- We extend the proposed method to video frame interpolation and prediction in a *zero-shot* manner, which formulates the reverse sampling of the diffusion model to build a unified event-to-frame reconstruction framework.

The rest of this paper is organized as follows: In Section 2, we review related work on event-based video frame reconstruction, interpolation, and prediction, and advancements in diffusion models. Section 3 introduces event representation and the diffusion model. In Section 4, we present the proposed method, including the event-conditioned fine-tuning of the diffusion model, inter-frame residual guidance, and adaptation to video frame interpolation and prediction. Section 5 presents detailed experimental settings, results, and comparisons with state-of-the-art methods. In Section 6, we conduct comprehensive ablation studies to verify the effectiveness of each component in our network. Finally, Section 7 concludes the paper and outlines potential future research directions.

## 2 Related Work

### Event-based Video Frame Reconstruction.

Event cameras offer unique advantages, including high dynamic range, high temporal resolution, and low power consumption [1, 2, 10, 33–35]. Existing event-based video frame reconstruction approaches can be broadly divided into two categories: diffusion-model-based methods and non-diffusion-based methods. Early non-diffusion methods relied on the intensity gradients provided by events and optical flow to reconstruct scene intensity [36–39]. Recently, deep learning has driven major advances: [9] pioneered the use of convolutional recurrent neural networks for high-quality reconstructions; FireNet [12] achieves faster inference with a lightweight design; [11] improved model generalization via data augmentation. By utilizing the self-supervised framework [40], spatially-adaptive denormalization [13], transformer models [14], and context-guided hypernetworks, these approaches have shown remarkable performance. For the

diffusion-based methods, based on the coarse reconstruction result from ETNet [14], [41] and [42] utilized a diffusion model [21] to enhance the high-frequency components of objects in reconstructed images. In addition, [43] leveraged language guidance and pretrained diffusion models to achieve semantic-aware event-to-video reconstruction. E2VIDiff [44] introduces diffusion models with event-guided sampling to reconstruct colorful and perceptually realistic videos from achromatic event streams. CUBE [45] utilizes the edge information from events and combined it with textual descriptions to guide the diffusion network to synthesize videos in a zero-shot manner.

In contrast to these methods, which are limited to reconstructing video frames from events, our UniE2F, leveraging rich pre-trained generative priors and score function modulation, not only reconstructs video frames in real-world scenes from event inputs, but also performs video frame interpolation and future-frame prediction in a zero-shot manner, without any additional training.

#### **Event-based Video Frame Interpolation.**

Due to the high temporal resolution and low latency of event data, it has been utilized to interpolate intermediate frames to achieve accurate and temporally consistent video frame reconstruction. Time Lens [17] introduces a unified CNN framework that combines event-based motion estimation with both warping- and synthesis-based interpolation to robustly generate high-quality frames under non-linear motion, motion blur, and illumination changes. Then, in Time Lens++ [46], the motion spline estimator and multi-scale feature fusion module were proposed to achieve temporally consistent interpolation and reduce ghosting artifacts. [47] utilized the continuous trajectory guided motion estimation module to track the continuous motion trajectory of each divided patch. TimeLens-XL [48] decomposes large inter-frame displacements into multiple small-step motions and recursively estimates the optical flow at each step using events, enabling tracking of nonlinear motion. Additionally, CBM-Net [49] was proposed to leverage cross-modal asymmetric bidirectional motion fields from events and images to interpolate video frames without motion approximations. Based on the pretrained diffusion model, [50] trained a trainable copy on a

real-world and event-based interpolation dataset in order to control the diffusion network to synthesize intermediate frames.

Distinct from previous work, we propose a new paradigm that simply modulates the reverse diffusion sampling process to transfer reconstruction priors to interpolation and prediction in a zero-shot manner. By fully leveraging event streams, this unified paradigm completes event-driven reconstruction, interpolation, and prediction without task-specific datasets or complex network designs.

**Diffusion Model.** Denoising Diffusion Probabilistic Model (DDPM) [21] has demonstrated remarkable success in image synthesis, with its capability evidenced by generating high-quality images from random noise. The Latent Diffusion Model (LDM) [28] performs forward and reverse diffusion processes on the latent space, significantly enhancing efficiency in high-resolution image synthesis. Following LDM, [28] introduced DiffIR [51], applying diffusion on a compact prior representation to achieve more efficient and stable image restoration. To enable high-resolution video generation, [52] developed video LDM by introducing a temporal dimension to the pre-trained image LDM [28] and fine-tuning it on video data. Subsequently, the SVD model is accomplished by pretraining video LDM [52] on well-curated datasets and pipelines, resulting in significant performance improvements for high-quality video generation.

**Event Stacking Approaches.** To convert the asynchronous event stream into a tensor suitable for convolutional networks, a common practice is to partition it into temporal bins, accumulate events in each bin to form “event frames,” and stack these along the channel dimension into an event volume. [53] first systematically introduced time-based and event-count-based stacking strategies (SBT/SBE) for event-based HDR and high frame-rate video reconstruction, establishing the basic form of event stacking; [54] proposed mixed-density stacks in stereo event-based depth estimation to balance short-term details and long-term context; [55] further modeled bidirectional event summations as a learnable Neural Event Stack for image enhancement, alleviating the sensitivity of hand-crafted stacks to noise.

### 3 Preliminary

**Event Representation.** Given the event stream  $\{e_i\}_{i=0}^{N_E-1}$  containing  $N_E$  events over a duration of  $T$  seconds, each event data  $\{e_i\}_{i=0}^{N_E-1}$  is encoded in the format of  $e_i = (x_i, y_i, t_i, p_i)$ , where  $x_i$ ,  $y_i$ ,  $t_i$  and  $p_i$  denote the pixel positions, timestamp, and the polarity of intensity change. Notably,  $x_i \in \{0, \dots, W - 1\}$ ,  $y_i \in \{0, \dots, H - 1\}$ ,  $t_i \in [0, T]$ ,  $p_i \in \{+1, -1\}$  for all  $i \in \{0, \dots, N_E - 1\}$ , where  $H$  and  $W$  denote the height and width of the sensor array of an event camera. Due to the sparse and asynchronous characteristics of the event stream, a typical preprocessing approach in previous work [9, 11, 14] is to accumulate the sequence of event data into a 2D image-like tensor representation, allowing its compatibility with frame-based reconstruction algorithms. Specifically, let us  $\mathbf{V} \in \mathbb{R}^{F \times 3 \times H \times W}$  denote the sequence of  $F$  video frames to be reconstructed, and let  $\{s_f\}_{f=0}^{F-1}$  be the corresponding timestamps, uniformly distributed over the same duration of  $T$  seconds. By setting  $s_{-1} = 0$ , we distribute the continuous events between two adjacent frames into the group  $\mathcal{G}_f = \{e_i \mid s_{f-1} \leq t_i < s_f\}$ , where  $\mathcal{G}_f$  denotes the  $f$ -th group of events that spans a duration of  $\Delta T$  seconds. Then, to leverage the rich generative prior of the pre-trained diffusion model developed on 3-channel RGB frames, we transform  $F$  event groups into the sequence of 3-channel event representations also with the number of  $F$ , which is denoted as  $\mathbf{E} \in \mathbb{R}^{F \times 3 \times H \times W}$ . For each event representation  $\mathbf{E}_f$  ( $f \in \{0, \dots, F - 1\}$ ), we encode the event data  $\mathcal{G}_f$  into three channels corresponding to (i) the sum of all events, (ii) the sum of positive events only, and (iii) the sum of negative events only.

**Diffusion Model.** As a type of generative model, the diffusion model [21] first utilizes a forward diffusion process to transform data from complex high-dimensional distributions to simpler ones (typically Gaussian) and then applies the reverse diffusion process to reconstruct the original data distribution from the simplified one. According to [56], the forward stochastic differential equation (SDE) process of the latent diffusion model [28] can be formulated as

$$d\mathbf{x} = f(t)\mathbf{x}dt + g(t)d\mathbf{w}, \quad (1)$$

where  $\mathbf{x} \in \mathbb{R}^n$  is the noised latent state,  $\mathbf{w} \in \mathbb{R}^n$  represents a standard Wiener process,  $t$  indicates the diffusion timestamp,  $f(t)$  and  $g(t)$  yield the drift and diffusion coefficients, which indicate the variation of data and noise components during the diffusion process. Therefore, the reverse process of the latent diffusion model [28] can be formulated via the ordinary differential equation (ODE) solution [57]:

$$d\mathbf{x} = \left[ f(t)\mathbf{x} - \frac{1}{2}g^2(\mathbf{x})\nabla_{\mathbf{x}} \log q_t(\mathbf{x}) \right] dt, \quad (2)$$

where  $\nabla_{\mathbf{x}} \log q_t(\mathbf{x})$  is usually approximated through training a score model  $\mathcal{S}_\theta(\mathbf{x}, t)$  with parameter  $\theta$ . Taking into account the special case of the variance exploding (VE) diffusion process [56] of the SVD model, the reverse process can be simplified as

$$\mathbf{x}^{t-1} = \mathbf{x}^t - \frac{\mathbf{x}^t - \mathbf{u}^t}{\sigma_t}(\sigma_t - \sigma_{t-1}), \quad (3)$$

where  $\mathbf{u}^t = \mathcal{X}_\theta(\mathbf{x}^t, t)$  represents the estimated clean latent from the noised latent  $\mathbf{x}^t \sim \mathcal{N}(\mathbf{x}^0, \sigma_t^2 \mathbf{I})$  at step  $t$  by the denoising U-Net  $\mathcal{X}_\theta(\cdot)$ , and  $\sigma_t$  is the variance of the Gaussian noise in the diffusion process.

### 4 Proposed Method

Leveraging the strong generative prior of the pre-trained SVD model, we first reconstruct video frames solely from the event representation  $\mathbf{E}$ . When the first and/or last frames (optionally) of the ground-truth sequence  $\mathbf{V}$  become available, we seamlessly adapt this event-driven reconstruction to frame interpolation and prediction in a zero-shot fashion, yielding a unified framework for event-to-frame (UniE2F), as illustrated in Fig. 2. Technically, we first introduce a baseline event-based video frame reconstruction model by fine-tuning the SVD model using event representations as conditional inputs, providing a foundation for the subsequent design (Sec. 4.1). Then, we present the inter-frame residual guidance (Sec. 4.2). Finally, we modulate the score function to enable the adaptation to video frame interpolation and prediction in a *zero-shot* manner (Sec. 4.3).

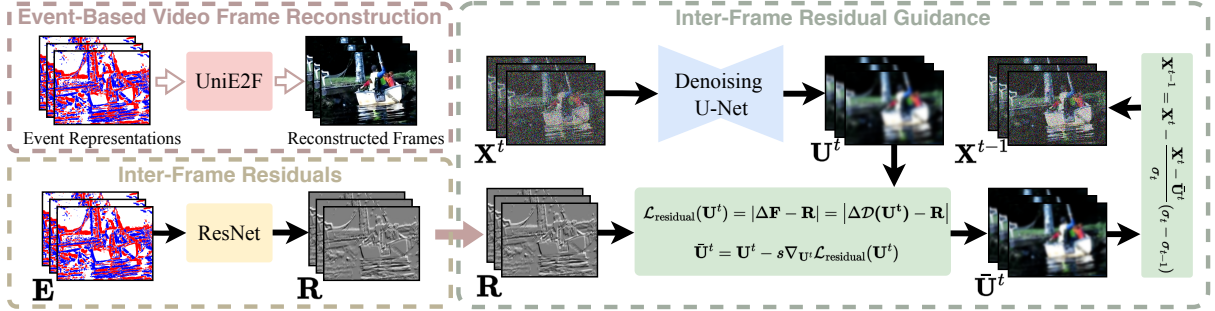


**Fig. 2:** The schematic of the proposed framework, which integrates event-based inter-frame residual guidance during the inference stage. At step  $t$  ( $t \leq \tau$ ), given event representations, we utilize a ResNet to predict the inter-frame residuals between consecutive frames. Then, these residuals are utilized to formulate the inter-frame residual loss  $\mathcal{L}_{\text{residual}}$ , which is optimized via a gradient descent algorithm to update noisy latent.

#### 4.1 Fine-tuning with Event Representation

To leverage the high temporal resolution property of event data to guide the pre-trained diffusion model with large generative priors for video frame reconstruction, we propose an event-conditioned fine-tuning strategy. Specifically, we first encode the event representation  $\mathbf{E}$  with a dedicated encoder  $\mathcal{E}(\mathbf{E})$  that serves as the conditioning input. Subsequently, following the training scheme in previous works [56–58], at each diffusion step  $t$  we randomly select a noisy latent  $\mathbf{X}^t \in \mathbb{R}^{F \times C \times H \times W}$  — and, for notational simplicity, treat both the latent and the video frame tensors as having the same size. Conditioned on the event representation, the denoising U-Net predicts the noise component  $\epsilon$  to estimate the clean latent  $\mathbf{U}^t = \mathcal{X}_\theta(\mathbf{X}^t, \mathcal{E}(\mathbf{E}), t)$ . Then the diffusion model is fine-tuned by minimizing the discrepancy between the estimated clean latent  $\mathbf{U}^t \in \mathbb{R}^{F \times C \times H \times W}$  and the ground truth clean latent  $\mathbf{X}^0 = \mathcal{E}(\mathbf{V})$ , with the loss function  $\mathcal{L}_{\text{fine-tuning}}$  formulated as

$$\mathcal{L}_{\text{fine-tuning}} = \mathbb{E}_t \left\{ \lambda(t) \mathbb{E}_{\mathbf{X}^0} \mathbb{E}_{\mathbf{X}^t | \mathbf{X}^0} \left[ \|\mathbf{X}^0 - \mathbf{U}^t\|_2^2 \right] \right\},$$

$$\lambda(t) = \frac{\sigma_t^2 + \sigma_{\text{data}}^2}{(\sigma_t + \sigma_{\text{data}})^2},$$
(4)

where  $\lambda(t)$  serves as a weighting function. Benefiting from this fine-tuning process, the pre-trained video diffusion model can effectively integrate

event data, thereby enabling a high-fidelity synthesis of dynamic visual content.

#### 4.2 Inter-Frame Residual Guidance

Observing that each event is triggered when pixel intensity changes reach a specific threshold, a notable correlation exists between the accumulated events and the corresponding inter-frame residual at the same pixel. However, due to the differences in sensor sensitivities, gamma correction, or other ISP algorithms, it is intractable to manually solve the inverse process that directly calculates the frame residual. Thus, we propose to leverage event representations to predict inter-frame residuals, employing these residuals as denoising guidance to balance reconstruction fidelity and diversity in the last  $\tau$  steps.

Based on the reverse diffusion sampling process described in Eq. (3), we obtain the differential update of the latent as

$$\mathbf{X}^{t-1} = \mathbf{X}^t - \frac{\mathbf{X}^t - \mathbf{U}^t}{\sigma_t} (\sigma_t - \sigma_{t-1}).$$
(5)

As illustrated in Fig. 2, we initially train an off-the-shelf ResNet [59] model to map the event representation  $\mathbf{E}$  to the inter-frame residual  $\mathbf{R}$ . Subsequently, at step  $t$  ( $t \leq \tau$ ) of the reverse diffusion process, the estimated clean latent  $\mathbf{U}^t$  — derived from  $\mathbf{X}^t$  — is fed into the autoencoder’s decoder  $\mathcal{D}$  to produce the estimated clean frame  $\mathbf{F} = \mathcal{D}(\mathbf{U}^t)$ . The residual between each frame  $\mathbf{F}$  and its preceding frame is calculated to obtain  $\Delta \mathbf{F}$ . We then compute the inter-frame residual

loss function, which is formulated based on the L1 distance between the predicted inter-frame residual  $\mathbf{R}$  and the residual derived from the estimated clean frame  $\Delta\mathbf{F}$  in pixel space, i.e.,

$$\mathcal{L}_{\text{residual}}(\mathbf{U}^t) = |\Delta\mathbf{F} - \mathbf{R}| = |\Delta\mathcal{D}(\mathbf{U}^t) - \mathbf{R}|. \quad (6)$$

This loss function is optimized via the gradient descent algorithm to update the estimated clean latent  $\mathbf{U}_t$  at each sampling step  $t$ :

$$\bar{\mathbf{U}}^t = \mathbf{U}^t - s\nabla_{\mathbf{U}^t}\mathcal{L}_{\text{residual}}(\mathbf{U}^t), \quad (7)$$

where  $s$  is the coefficient that controls the strength of the guidance. Moreover, in the following Proposition, we theoretically validate that our regularization in Eq. (7) does not degrade generation quality and that minimizing such regularization can indeed improve generation quality by minimizing the potential error upper boundary.

**Proposition 1** The gradient term  $\nabla_{\mathbf{U}^t}\mathcal{L}_{\text{residual}}(\mathbf{U}^t)$  derived from the inter-frame residual guidance lies in the tangent space  $T_{\mathbf{U}^t}\mathcal{M}$  of the data manifold  $\mathcal{M}$  learned by the diffusion model. Then, we have the following characteristics:

- It ensures the updated latent  $\bar{\mathbf{U}}^t = \mathbf{U}^t - s\nabla_{\mathbf{U}^t}\mathcal{L}_{\text{residual}}$  remains on  $\mathcal{M}$ ; and
- The reconstruction error is bounded by  $\frac{L\kappa}{C}\mathcal{L}_{\text{residual}} + \frac{F\varepsilon}{C}$ .

Geometrically, the gradient of the residual loss lies in the tangent space of the data manifold because, during posterior sampling, the diffusion model’s denoising trajectory follows the radial direction (normal to the manifold) to reach valid data points. In contrast, our residual guidance operates tangentially-searching along the manifold’s surface to find samples that satisfy the inter-frame physical constraints without leaving the space of plausible images.

*Proof* See Appendix A.  $\square$

By substituting the original  $\mathbf{U}_t$  in the reverse diffusion Eq. (5) with the refined clean latent expectation term, the sampling process is guided as follows:

$$\mathbf{X}^{t-1} = \mathbf{X}^t - \frac{\mathbf{X}^t - \bar{\mathbf{U}}^t}{\sigma_t}(\sigma_t - \sigma_{t-1}). \quad (8)$$

---

### Algorithm 1 Reverse Diffusion Sampling for Video Frame Interpolation and Prediction

---

- 1: **input:** clean latents  $\{\mathcal{E}(\mathbf{V}_0), \mathcal{E}(\mathbf{V}_{F-1})\}$  (resp.  $\{\mathcal{E}(\mathbf{V}_0)\}$ ) for the task of video frame interpolation (resp. prediction), diffusion U-Net  $\mathcal{X}_\theta(\cdot)$ , encoded event representation  $\mathcal{E}(\mathbf{E})$ .
  - 2: initialize  $\mathbf{X}^T \sim \mathcal{N}(\mathbf{0}, \sigma_i\mathbf{I})$ .
  - 3: **for**  $t = T, \dots, 1$  **do**
  - 4:   forward  $\mathbf{U}^t = \mathcal{X}_\theta(\mathbf{X}^t, \mathcal{E}(\mathbf{E}), t)$ .
  - 5:   **for**  $i = 0, \dots, F - 1$  **do**
  - 6:     **if** *video frame interpolation* **then**
  - 7:       calculate  $\bar{\mathbf{U}}^t$  via Eq. (10),
  - 8:     **else if** *video frame prediction* **then**
  - 9:       calculate  $\bar{\mathbf{U}}^t$  via Eq. (12),
  - 10:    **end if**
  - 11:    reverse  $\mathbf{X}^t$  to  $\mathbf{X}^{t-1}$  via Eq. (11).
  - 12:   **end for**
  - 13: **end for**
  - 14: **return** reconstructed latent  $\mathbf{X}^0$ .
- 

### 4.3 Adaptation to Video Frame Interpolation and Prediction

Through the training on the event-based video frame reconstruction task, our approach is expected to acquire a powerful generative capability to map sparse, asynchronous event data to realistic and continuous video frames. Exploiting this ability, we extend our method to video frame interpolation and prediction without additional fine-tuning. Specifically, for video frame interpolation (or prediction), by leveraging the prior information from the first and last reference frames (or solely the first frame), we modulate the score function to theoretically reformulate the reverse diffusion sampling during the inference phase. This revised formulation then guides the video diffusion model to reconstruct the intermediate (or subsequent) frames with enhanced temporal consistency and visual fidelity.

Here, we take video frame interpolation as an example to illustrate our approach. Given the clean latents  $\mathcal{E}(\mathbf{V}_0)$  and  $\mathcal{E}(\mathbf{V}_{F-1})$ , obtained by feeding the first and last video frames into the autoencoder’s encoder, we first compute the deviations between them and the corresponding

intermediate estimations  $\mathbf{U}_0^t$  and  $\mathbf{U}_{F-1}^t$ :

$$\begin{aligned}\mathbf{D}_0^t &= \mathcal{E}(\mathbf{V}_0) - \mathbf{U}_0^t, \\ \mathbf{D}_{F-1}^t &= \mathcal{E}(\mathbf{V}_{F-1}) - \mathbf{U}_{F-1}^t.\end{aligned}\quad (9)$$

Since these deviations are highly correlated with the discrepancy between the estimated clean latents and the provided prior information, an effective score function can be designed by utilizing  $\mathbf{D}_0^t$  and  $\mathbf{D}_{F-1}^t$  modulating the estimated latent representation  $\mathbf{U}_i^t$  for  $0 \leq i \leq F-1$ . Thus, the score function of the reverse diffusion sampling is formulated:

$$\begin{aligned}\tilde{\mathbf{U}}_i^t &= \alpha(t) \left[ \frac{(\mathbf{D}_0^t + \mathbf{U}_i^t) + (\mathbf{D}_{F-1}^t + \mathbf{U}_i^t)}{2} \right] \\ &\quad + [1 - \alpha(t)]\mathbf{U}_i^t\end{aligned}\quad (10)$$

where the weighting coefficient  $\alpha(t) = 1 - e^{-\sigma t}$  balances the influence of the deviation correction. To guide the reverse sampling of the video diffusion model, we replace  $\mathbf{U}^t$  in Eq. (5) with the optimized clean latent expectation term  $\tilde{\mathbf{U}}_i^t$ :

$$\mathbf{X}^{t-1} = \mathbf{X}^t - \frac{\mathbf{X}^t - \tilde{\mathbf{U}}^t}{\sigma_t}(\sigma_t - \sigma_{t-1}).\quad (11)$$

It is important to note that for video frame prediction, only  $\mathcal{E}(\mathbf{V}_0)$  is available. In this case, the score function is modified into

$$\tilde{\mathbf{U}}_i^t = \alpha(t)(\mathbf{D}_0^t + \mathbf{U}_i^t) + [1 - \alpha(t)]\mathbf{U}_i^t.\quad (12)$$

Alg. 1 summarizes the reverse diffusion sampling process.

## 5 Experiment

### 5.1 Experiment Settings

**Dataset.** The training set was generated by synthesizing event-frame pairs from real-world videos. Specifically, 1,800 sequences (400–500 frames each) were drawn from TrackingNet [60], and event stream between consecutive frames was simulated with DVS-Voltmeter [61]. For evaluation, we constructed a synthetic test set of 212 sequences from TrackingNet [60] and a real-world test set of 107 sequences from HS-ERGB [17], each containing 12 frames. More details of the dataset are provided in Appendix B.

**Implementation Details.** All the experiments were conducted on an NVIDIA RTX A6000 GPU. In our experiments, the denoising U-Net architecture was initialized using the pre-trained weights of the SVD model. During training, we selectively fine-tuned the temporal transformer blocks while keeping all other parameters frozen, ensuring effective adaptation to the event-based domain. The network was optimized for 450,000 iterations using the AdamW optimizer [63] with a learning rate of  $1 \times 10^{-5}$ . In both the training and inference stages, we set  $F = 12$  and employed 30 diffusion steps for the inference phase, with our event-based inter-frame residual guidance applied during the last 10 steps. Besides, we illustrate the training strategy for the inter-frame residual estimator in Appendix C. In terms of inference latency, reconstructing a sequence of 12 RGB frames with the resolution of  $448 \times 320$  takes about 48 seconds. To quantitatively evaluate the model’s performance, we employ three widely used metrics: MSE (lower is better), SSIM [64] (higher is better), and LPIPS [65] (lower is better).

### 5.2 Results of Event-based Frame Reconstruction

**Comparison on Synthetic and Real-World Datasets.** We compared our method against various event-based reconstruction approaches, employing their official implementations and pre-trained parameters to ensure a fair evaluation. Notably, since the methods in [41], [42], and [43] were not open-sourced, and therefore they could not be included in our comparison. The quantitative results, as summarized in Table 1, reveal that our approach consistently outperforms the compared methods across multiple metrics. Specifically, our method outperforms state-of-the-art approaches, achieving the lowest MSE of 0.0612 and the highest SSIM of 0.4990 on the real-world dataset. Similar advantages are observed on the synthetic dataset, where our approach yields significant performance gains across the same evaluation metrics. Qualitative comparisons illustrated in Figure 3 (with more visual comparison results provided in Appendix D) reveal that our UniE2F, leveraging a large-scale generative prior along with inter-frame residual guidance, achieves reconstruction with improved color fidelity and

**Table 1:** Quantitative comparison with state-of-the-art event-based video frame reconstruction methods on real-world and synthetic datasets. The best result in each column is highlighted in **bold**.

Method	Real-World			Synthetic		
	MSE ↓	SSIM ↑	LPIPS ↓	MSE ↓	SSIM ↑	LPIPS ↓
E2VID [9]	0.1275	0.4200	0.6210	0.0678	0.5040	0.5420
FireNet [12]	0.1210	0.4110	0.6300	0.0620	0.5560	0.5220
E2VID+ [11]	0.0650	0.4390	0.6180	0.0550	0.5130	0.5430
FireNet+ [11]	0.0737	0.3870	0.6620	0.0581	0.4540	0.5790
ETNet [14]	0.0849	0.4230	0.6440	0.0522	0.5110	0.5480
SSL-E2VID [40]	0.1008	0.3660	0.6260	0.0694	0.4980	0.6510
SPADE-E2VID [13]	0.0727	0.4330	0.5990	0.0992	0.4500	0.6340
CUBE [45]	0.0851	0.3640	0.6900	0.1437	0.1920	0.7970
HyperE2VID [62]	0.0632	0.4770	<b>0.5620</b>	0.0727	0.3860	0.6320
<b>UniE2F (Ours)</b>	<b>0.0612</b>	<b>0.4990</b>	0.6740	<b>0.0167</b>	<b>0.7100</b>	<b>0.3940</b>



**Fig. 3:** Visual comparison of event-based video frame reconstruction results on synthetic (1st and 2nd rows) and real-world (3rd and 4th rows) datasets. The event data is visualized as a polarity map.

fewer artifacts. In contrast, the compared methods, trained on grayscale images, tend to produce monochromatic outputs inconsistent with real-world color scenes, suffer from significant detail loss, and exhibit obvious artifacts.

*It is worth noting* that although our method yields more natural and realistic reconstruction, a noticeable discrepancy in color tone remains between our result and the ground truth. This is primarily because event streams capture only intensity changes and inherently lack color information. Without the prior information about the colors of the scenes, achieving perfectly consistent color restoration remains an inherently challenging and ill-posed problem.

**Comparison on HQF, IJRR, and MVSEC Datasets.** We further compare UniE2F qualitatively with existing methods on three widely used real-world datasets: HQF [11], IJRR [67], and MVSEC [68], which provide single-channel intensity frames as ground truth. As shown in Figure 5, our UniE2F can reconstruct frames with more realistic colors and clear details, making them closer to real scenes. In contrast, the other methods can only produce single-channel grayscale reconstructions, which lack color information and look less natural.

**Table 2:** Quantitative comparison for video frame interpolation (VFI) and video frame prediction (VFP). The best result in each column is highlighted in **bold**. Here, “†” denotes the model with pretrained weight and “\*” denotes the model retrained on our synthetic dataset.

Method	Mode	Synthetic			Real-World		
		MSE ↓	SSIM ↑	LPIPS ↓	MSE ↓	SSIM ↑	LPIPS ↓
CBMNet† [49]	VFI-4×	0.0250	0.5860	<b>0.3030</b>	0.0032	0.8230	<b>0.2540</b>
CBMNet* [49]	VFI-4×	0.0174	0.6320	0.3550	<b>0.0023</b>	<b>0.8360</b>	0.2810
TimeLens-XL† [48]	VFI-4×	0.0321	0.5350	0.3270	0.0080	0.7270	0.2920
TimeLens-XL* [48]	VFI-4×	0.0291	0.5480	0.3160	0.0078	0.7270	0.2900
<b>UniE2F (Ours)</b>	VFI-4×	<b>0.0063</b>	<b>0.7340</b>	0.3210	0.0041	0.6770	0.4310
CBMNet† [49]	VFI-11×	0.0491	0.4040	0.4580	0.0892	0.5120	0.5800
CBMNet* [49]	VFI-11×	0.0392	0.4530	0.5270	0.0063	<b>0.7500</b>	0.4000
RE-VDM† [50]	VFI-11×	0.0503	0.4180	0.4130	<b>0.0057</b>	0.7330	<b>0.3480</b>
<b>UniE2F (Ours)</b>	VFI-11×	<b>0.0072</b>	<b>0.7400</b>	<b>0.3200</b>	0.0058	0.6500	0.4000
Zhu et al.[66]†	VFP	0.0184	0.6140	0.3960	<b>0.0077</b>	<b>0.6620</b>	<b>0.3400</b>
<b>UniE2F (Ours)</b>	VFP	<b>0.0093</b>	<b>0.7100</b>	<b>0.3470</b>	0.0100	0.5940	0.4110

### 5.3 Results of Video Frame Interpolation and Prediction

Here, we conducted experiments to evaluate the *zero-shot* capability of our UniE2F on the event-based video frame interpolation and prediction tasks. Specifically, we defined three tasks: VFI-4×, VFI-11×, and VFP, which respectively increased the frame rate to 4 times and 11 times the original and predicted subsequent frames given the first frame. Following the above setup, we compared our method with several representative baselines for interpolation using their official pretrained weights or retraining them on our synthetic training set. Since TimeTracker [47] had *not been open-sourced*, its weights and results could not be obtained and were therefore omitted. More detailed descriptions of the experimental setting are provided in Appendix E.

The quantitative and qualitative results are presented in Table 2 and Figure 4, respectively. On the synthetic dataset, UniE2F delivers a clear advantage in both short-range and long-range interpolation as well as prediction, consistently outperforming all pretrained and retrained methods. On the real-world datasets, UniE2F shows relatively weaker quantitative performance compared to retrained baselines, which is mainly attributed to the domain gap between synthetic training and real-world event distributions. Nevertheless, considering that our model operates in a strict zero-shot setting without any fine-tuning on real-world data, its ability to remain competitive on unseen real-world interpolation

and prediction tasks is highly encouraging. Moreover, beyond numerical scores, UniE2F preserves motion dynamics while maintaining high-fidelity color, texture, and structural details, whereas outputs of other methods exhibit artifacts and degradation due to the lack of generative priors. Remarkably, these zero-shot results are obtained **without any fine-tuning on interpolation or prediction datasets**, which confirms that UniE2F provides a unified and flexible framework that not only delivers excellent performance in event-driven frame reconstruction but also delivers outstanding zero-shot performance on both interpolation and prediction tasks, highlighting its generalization strength and practical utility.

## 6 Ablation Study

**Guidance Strength Strategy.** We further investigated the optimal guidance strength strategy by evaluating four scheduling approaches under the experimental setup where the guidance was applied exclusively during the final 10 sampling steps. Specifically, we designed four scheduling strategies over the designated steps: **(1)** a baseline configuration with no guidance, i.e., the guidance strength was set to 0; **(2)** maintaining a constant guidance strength of 0.1; **(3)** linearly decreasing the guidance strength from 0.1 to 0, and **(4)** linearly increasing the guidance strength from 0 to 0.1. The comparison results Table 3 show that the linearly decreasing schedule (0.1 → 0.0) achieves the best performance compared with other configurations. The results indicate that



**Fig. 4:** Visual comparison on synthetic dataset: UniE2F is shown in both video frame interpolation (VFI) and video frame prediction (VFP) modes, while CBMNet is shown under the VFI setting. Note that the frames highlighted with purple borders denote the given frames, whereas frames highlighted with blue borders denote the predicted frames.

**Table 3:** Comparison of different guidance strength strategies.

Guidance Strength	Synthetic		
	MSE ↓	SSIM ↑	LPIPS ↓
0.0 → 0.0	0.0191	0.6880	0.4020
0.1 → 0.1	0.0234	0.6610	0.4190
0.0 → 0.1	0.0234	0.6540	0.4210
0.1 → 0.0	<b>0.0167</b>	<b>0.7100</b>	<b>0.3940</b>

applying stronger guidance early in the reverse diffusion process helps to enforce accurate inter-frame residual alignment, while gradually reducing the guidance allows the model’s generative prior to effectively refine finer details and prevent over-constraining the reconstruction. This progressive relaxation appears critical for balancing reconstruction fidelity with visual diversity.

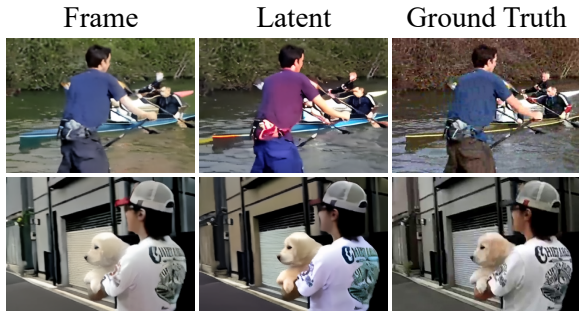
**Guidance Mode.** Since the SVD model conducts the denoising process in the latent space, a direct strategy to enhance inter-frame consistency is to impose explicit constraints on the residuals between adjacent frames within this space. To this end, we trained a ResNet with the aim of predicting inter-frame residuals within latent representation. As shown in Figure 6 and Table 4, the results of latent-level guidance are inferior to frame-level guidance results. Moreover, the images generated with frame-level guidance exhibit higher fidelity and richer details, producing sharper structures and more natural textures. In contrast, the outputs under latent-level guidance often suffer from noticeable distortions and artifacts, leading to degraded perceptual quality. The performance gap can be attributed to the Gaussian distribution inherent in the latent inter-frame residuals, making it particularly challenging



Fig. 5: Qualitative Comparison on HQF [11], IJRR [67], and MVSEC [68].

**Table 4:** Quantitative comparison of different guidance modes.

Guidance Mode	Synthetic		
	MSE ↓	SSIM ↑	LPIPS ↓
Latent	0.0197	0.6920	0.4060
Frame	<b>0.0167</b>	<b>0.7100</b>	<b>0.3940</b>



**Fig. 6:** Visual comparison of different guidance modes.

for networks trained with MAE loss to accurately model the precise variations.

**Max Guidance Strength.** The value of the weighting coefficient  $s$  controls the gradient update magnitude for the estimated clean latent  $U_t$  by weighting the contribution of the inter-frame residual loss. In the ablation experiments for the video frame reconstruction task, to evaluate the effect of the weighting coefficient  $s$ , we expanded the maximum guidance strength from 0.1 to larger values such as 0.5, 1.0, 5.0 and 10.0, and compared MSE, SSIM, and LPIPS (see Table 5). The results show that as the coefficient grows, MSE increases, SSIM drops, and LPIPS rises—indicating that overly strong residual guidance causes the reconstruction to depend too heavily on the event-frame residual. Because the mapping from events to RGB involves nonlinear steps (e.g., gamma correction, ISP pipeline) and is not one-to-one, amplifying this loss instead introduces artifacts and degrades visual quality.

**Inter-Frame Residual Guidance.** To demonstrate the effectiveness of the Inter-Frame Residual Guidance (IFRG), we have included a visual comparison in Figure 7. As shown, without IFRG (top row), the reconstructions exhibit noticeable blurring and structural distortion: the bars of the fence are wavy and over-smoothed, and the

**Table 5:** Quantitative comparison of different maximum guidance strength, evaluated using MSE, SSIM, and LPIPS.

Maximum Guidance Strength	Synthetic		
	MSE ↓	SSIM ↑	LPIPS ↓
10.0	0.0964	0.2950	0.7070
5.0	0.0573	0.4140	0.6510
1.0	0.0228	0.6140	0.4770
0.5	0.0188	0.6710	0.4240
0.1	<b>0.0167</b>	<b>0.7100</b>	<b>0.3940</b>



**Fig. 7:** Effect of Inter-Frame Residual Guidance (IFRG). Compared with the baseline (top), adding IFRG (middle) yields sharper edges and more faithful textures that better match the ground truth (bottom).

ground textures are largely washed out. With IFRG (middle row), edges and fine structures align much better with the ground truth (bottom row): the fence bars are straighter and more regular, and the sand and background textures are more faithfully recovered. These improvements indicate that IFRG effectively constrains the reconstruction with inter-frame intensity changes, yielding frames that are both structurally more accurate to the ground truth.

**Robustness to Event Noise.** We followed the setting in the SVD model, wherein the inference stage Gaussian noise with standard deviation 0.02 was injected into the 3-channel event representation. As a reference, we regarded this original noise injection scheme as the *Baseline*. To further evaluate the robustness of our network to

**Table 6:** Quantitative comparison of different noise-level coefficients, evaluated using MSE, SSIM, and LPIPS. The results demonstrate that our method exhibits strong robustness to event noise.

Noise-level Coefficient	Synthetic		
	MSE ↓	SSIM ↑	LPIPS ↓
1.0	0.0193	0.6690	0.4280
0.5	0.0177	0.6930	0.4050
0.1	0.0168	0.7080	0.3950
Baseline	<b>0.0167</b>	<b>0.7100</b>	<b>0.3940</b>

event noise, we introduced a noise-level coefficient  $\alpha$  to scale the noise strength relative to the standard deviation of the event representation  $E$ :  $E^{\text{noisy}} = E_{f,c,y,x} + \mathcal{N}(0, (\alpha \times \sigma_E)^2)$ ,  $\sigma_E = \text{std}(E)$ . By varying  $\alpha$ , we systematically controlled the injected noise magnitude. From Table 6, we observe that even under strong noise ( $\alpha = 1.0$ ), the reconstruction quality only slightly degrades: MSE rises from 0.0167 to 0.0193, SSIM drops from 0.7100 to 0.6690, and LPIPS increases from 0.3940 to 0.4280. These marginal changes demonstrate that our method maintains strong robustness to event noise.

**Reconstruction under Sparse Event Streams.** To further analyze the limitations of event-based video reconstruction, we investigated the behavior of UniE2F and competing methods in scenarios with extremely sparse events. Figure 8 presents qualitative comparisons of reconstructed frames under such sparse-event conditions. As can be seen from the figure, when the event stream becomes highly sparse, all event-based frame reconstruction methods—including ours—can only reliably recover structures in the vicinity of pixels where events are triggered. Regions without event activity provide little or no informative signal, and therefore cannot be faithfully reconstructed by any of these approaches. This illustrates a fundamental limitation shared by event-only reconstruction methods: in the absence of sufficient event observations, the model is unable to infer fine-grained details in event-free areas.

**Guidance Strength Scheduling.** Here, we investigated three different guidance strength

**Table 7:** Quantitative comparison of different guidance strength strategies, evaluated using MSE, SSIM, and LPIPS.

Guidance Strength Strategy	Synthetic		
	MSE ↓	SSIM ↑	LPIPS ↓
Constant	0.0234	0.6610	0.4190
Exponential	0.0181	0.6960	0.3990
Linear	<b>0.0167</b>	<b>0.7100</b>	<b>0.3940</b>

strategies—linearly increasing, linearly decreasing, and constant guidance strengths—and the results show that the linearly decreasing schedule achieves the best performance. Here, to evaluate the robustness of this schedule, we introduced a non-linearly exponential decreasing strategy, where the guidance strength decreases from 0.1 to 0 following an exponential curve. The comparison results are presented in the Table 7. As shown, the linearly decreasing schedule still outperforms the exponentially decreasing one.

**Long-Sequence Event-Based Video Reconstruction.** To further evaluate our method on long sequences, we followed the same data collection setup in Section 5.1. The long-sequence synthetic test set was built by sampling 200 video sequences from TrackingNet [60], each containing 23 frames. For UniE2F, we processed the sequences using a sliding window approach. We first performed event-to-frame reconstruction on the first 12 frames of each sequence, obtaining a 12-frame reconstructed sequence. Then, starting from the 12th frame, we used the following events and applied our prediction mode to generate the subsequent 11 frames. We compared UniE2F with recent event-based video frame reconstruction methods on this setting. As shown in Table 8, our method achieves better performance across the reported metrics, indicating that UniE2F maintains stronger reconstruction quality and temporal stability even when the sequence length is increased.

**Perceptual Quality Evaluation via Fréchet Inception Distance.** The real-world datasets we used contained relatively few scenes, and the color distribution of HS-ERGB may not fully align with real-world conditions, leading to perceptual deviations from natural scenes. Since UniE2F was trained with RGB frames from real-world scenes

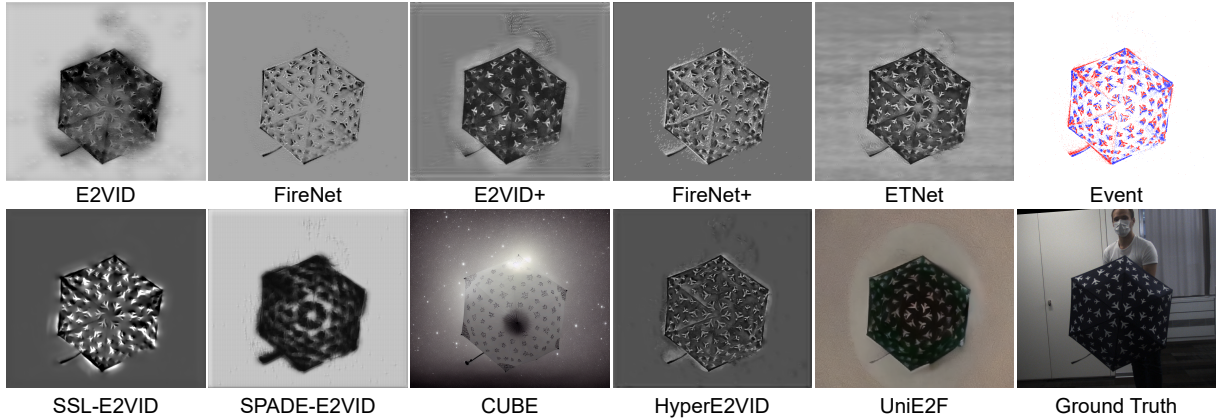


**Fig. 8:** Reconstruction under sparse event streams. All event-based methods recover structures near event pixels, but fail to reconstruct regions without events.

**Table 8:** Quantitative results for long-sequence generation on synthetic dataset.

Method	MSE ↓	SSIM ↑	LPIPS ↓
SSL-E2VID [40]	0.0906	0.4240	0.6310
SPADE-E2VID [13]	0.0682	0.5200	0.5680
HyperE2VID [62]	0.0591	0.4960	0.5700
<b>UniE2F (Ours)</b>	<b>0.0271</b>	<b>0.6530</b>	<b>0.4470</b>

in TrackingNet as supervisory targets, the color distribution of the reconstructed frames tends to be closer to real-world distributions, as seen in rows 3 and 4 of Figure 3. As a result, perceptual differences in high-dimensional feature spaces, such as those captured by LPIPS, may appear larger. Thus, here, we evaluated the reconstruction performance of our method and the competing approaches using the Fréchet Inception Distance (FID) metric (calculated via the Inception v3 network) as shown in the Table 9. As can be seen, our method outperforms the competitors in terms of FID [69], further supporting its advantages in generating perceptually high-quality reconstructions.

**Weighting Coefficient Scheduling.** In video frame interpolation tasks, we compared two weight-scheduling strategies: 1) Nonlinear schedule, as defined by the formula in the main text; 2) Linear schedule, i.e., linearly decreasing (increasing) from 1.0 (0.0) to 0.0 (1.0). The quantitative results are presented in Table 10. As shown in the

**Table 9:** Quantitative comparison of perceptual quality using FID (lower is better) for video frame reconstruction. UniE2F achieves the best FID, demonstrating its advantage in generating perceptually natural frames.

Method	Real-World	Synthetic
	FID ↓	FID ↓
E2VID [9]	223.7926	179.1581
FireNet [12]	241.5848	172.3014
E2VID+ [11]	240.4527	203.2372
FireNet+ [11]	250.4045	245.4307
ETNet [14]	252.4636	207.1250
SSL-E2VID [40]	252.2566	241.1340
SPADE-E2VID [13]	248.8114	193.7386
CUBE [45]	207.4970	192.1830
HyperE2VID [62]	272.1271	224.4130
<b>UniE2F (Ours)</b>	<b>184.2509</b>	<b>57.1092</b>

table, the nonlinear schedule generally achieves lower MSE and LPIPS scores while maintaining competitive SSIM, indicating a more effective fusion of reference-frame information compared to the linear schedule. In particular, the “Nonlinear 1.00 → 0.00” configuration yields the best overall performance, consistently reducing distortion and perceptual error. Therefore, comprehensively considering MSE, SSIM, and LPIPS, we adopt “Nonlinear 1.00 → 0.00” as the default setting.

**Video Frame Interpolation/Prediction without Event.** To illustrate the contribution of event data, we conducted experiments to evaluate

**Table 10:** Quantitative comparison of different weight-scheduling strategies for video frame interpolation (VFI), evaluated using MSE, SSIM, and LPIPS.

Mode	Weighting Coefficient	Synthetic		
		MSE ↓	SSIM ↑	LPIPS ↓
Linear	0.50 → 0.50	0.0080	0.7110	0.3460
Linear	0.00 → 1.00	0.0082	0.7030	0.3540
Linear	1.00 → 0.00	0.0076	<b>0.7450</b>	0.3220
Nonlinear	0.00 → 1.00	0.0090	0.6960	0.3630
Nonlinear	1.00 → 0.00	<b>0.0072</b>	0.7400	<b>0.3200</b>

**Table 11:** Quantitative comparison of UniE2F with and without event guidance for prediction and interpolation.

Task	MSE ↓	SSIM ↑	LPIPS ↓
Prediction (w/ Event)	<b>0.0093</b>	<b>0.7100</b>	<b>0.3470</b>
Prediction (w/o Event)	0.1563	0.107	0.658
Interpolation (w/ Event)	<b>0.0072</b>	<b>0.7400</b>	<b>0.3200</b>
Interpolation (w/o Event)	0.1437	0.119	0.633

the performance of UniE2F with only image input in interpolation and prediction tasks, i.e., without using events as conditional guidance. The qualitative results on synthetic datasets are shown in Table 11 and Figure 9. As can be seen from the table and figure, UniE2F has learned during training to map event representations to RGB frames. When we remove the event input and, following SVD, condition the model only on RGB frames that lie in a different domain, the network effectively applies this learned event-to-RGB mapping to RGB-to-RGB conditioning instead. This mismatch causes strong artifacts and disturbed appearance patterns. This demonstrates the critical role that event data plays in providing precise constraints, enabling the model to reconstruct intermediate or subsequent frames by adjusting the score function, even without explicit training for interpolation and prediction tasks.

**Event-Driven Interpolation at Arbitrary Timestamps.** Here, we provided the experiment to evaluate the interpolation capability of our UniE2F at arbitrary timestamps. Concretely, we took a sequence of 12 frames. Concretely, we

take a sequence of 12 frames  $\{V_0, V_1, \dots, V_{11}\}$  from the dataset and the 12 corresponding event groups  $\{\mathcal{G}_0, \mathcal{G}_1, \dots, \mathcal{G}_{11}\}$ . Then, for the interpolation task, we **focused only on the frames between the first and last frames**, i.e., the 10 event groups  $\{\mathcal{G}_1, \mathcal{G}_2, \dots, \mathcal{G}_{10}\}$  associated with  $\{V_1, V_2, \dots, V_{10}\}$ . These 10 intermediate event groups were re-partitioned into 7 new event groups, each covering a new temporal sub-interval between  $V_0$  and  $V_{10}$ . Together with the original event groups ( $\mathcal{G}_0$  and  $\mathcal{G}_{11}$ ) aligned with the first and last frames ( $V_0$  and  $V_{11}$ ), thus we can obtained a total of 9 event groups.

Under this setting, we applied the interpolation scheme conditioned on the new sequence of 9 event groups. As shown in Figure 10, UniE2F successfully reconstructs the video frame at the *end timestamp* of the intermediate event group, even though the temporal duration of this event group has been changed. This demonstrates that, by flexibly adjusting the temporal duration of the event group at inference time, our UniE2F can generate frames at arbitrary user-specified timestamps, rather than being restricted to a fixed, pre-defined set of timestamps.

**Table 12:** Comparison of computational overhead between our UniE2F and other methods, evaluated by reconstructing a sequence of 12 RGB frames at  $448 \times 320$  resolution.

Method	Computational Cost (TMACs)	Peak Memory Footprint (MB)
E2VID [9]	0.583	622
FireNet [12]	0.064	462
E2VID+ [11]	0.782	816
FireNet+ [11]	0.064	436
ETNet [14]	1.737	1074
SSL-E2VID [40]	0.065	640
SPADE-E2VID [13]	0.226	1096
CUBE [45]	300.116	8215
HyperE2VID [62]	0.060	1052
<b>UniE2F (Ours)</b>	344.34	46753

**Computational Overhead.** We evaluated the efficiency of our UniE2F and other methods on a single NVIDIA RTX A6000 GPU by reconstructing a sequence of 12 RGB frames at  $448 \times 320$  resolution. The result is listed in Table 12. Although

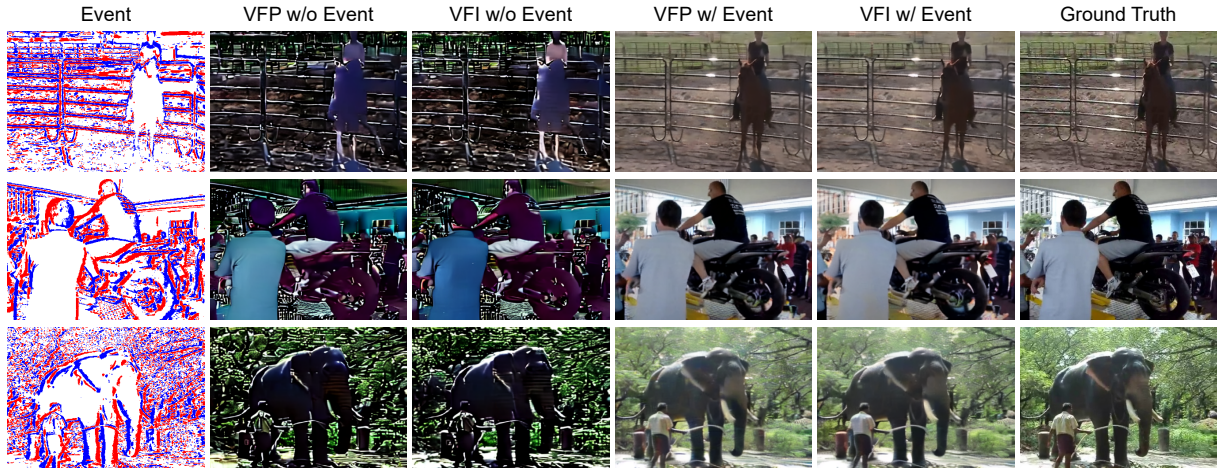


Fig. 9: Video frame interpolation/prediction without events.

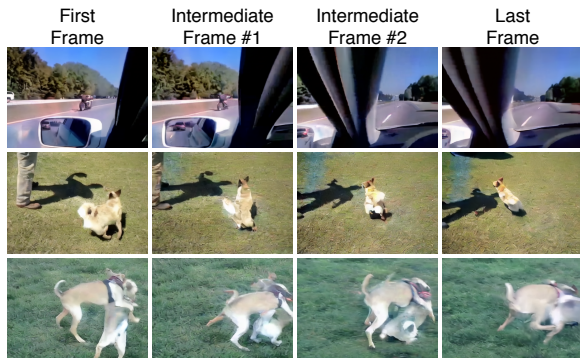


Fig. 10: Event-driven interpolation at arbitrary timestamps.

**Table 13:** Quantitative comparison of reconstruction performance and computational overhead of our method under different sampling steps.

Sampling Steps	Computational Cost (TMACs)	Synthetic		
		MSE ↓	SSIM ↑	LPIPS ↓
1	37.14	0.0197	0.6490	0.4380
5	77.13	0.0176	0.6760	0.4130
15	162.30	0.0168	0.6980	0.4000
30	344.34	<b>0.0167</b>	<b>0.7100</b>	<b>0.3940</b>

UniE2F’s use of a pre-trained stable video diffusion model’s generative prior incurs higher computational cost and GPU memory usage than non-diffusion methods, it provides a high-quality

baseline for event-to-frame reconstruction. Moreover, the Stable Diffusion-based CUBE requires both user-provided text prompts and event data, and its reconstruction fails when only pure events are supplied. By contrast, our method still significantly outperforms CUBE in reconstruction fidelity and visual quality even without any textual prompts.

It is important to note that computational efficiency is not the primary goal of our approach. Instead, since reconstructing video frames from events is a highly challenging information recovery task where significant visual details are missing, it inherently necessitates the integration of powerful generative priors. The core objective of this work is to investigate how to effectively leverage existing large-scale pretrained video diffusion models and transfer their powerful generative priors to event-based vision tasks, rather than restricting the discussion to comparisons under a fixed small-model computational budget. While utilizing such foundation models naturally raises concerns regarding computational complexity, we demonstrate that this can be alleviated by reducing the number of sampling steps to achieve a practical trade-off between efficiency and performance, as shown in Table 13. By reducing the number of sampling steps to 15, 5 and 1, the computational cost of our method significantly drops from 344.34 to 162.30, 77.13 and 37.14 TMACs, while still maintaining superior reconstruction fidelity compared to all other state-of-the-art methods for event-based video frame reconstruction. In future

work, building on the proposed UniE2F, we will investigate diffusion-model distillation and network pruning to further speed up inference for real-time applications.

## 7 Conclusion and Discussion

We have presented a novel event-based video frame reconstruction approach by fine-tuning a pre-trained SVD model with event data as conditional inputs. Leveraging the powerful generative prior from the pre-trained video diffusion model, our method significantly enhances the fidelity and realism of reconstructed frames, especially in complex dynamic scenes. The introduction of event-based inter-frame residual guidance further improves the accuracy while maintaining diversity in the reconstruction. Our unified framework is versatile, not only excelling in video frame reconstruction but also extending seamlessly to tasks such as interpolation and prediction. Experimental results on both synthetic and real-world datasets validate the effectiveness of our approach, demonstrating improved performance compared to existing methods across multiple evaluation metrics.

**Limitation and Future Work.** While UniE2F achieves high-quality reconstruction, its reliance on a large diffusion backbone incurs higher computational cost and memory usage than non-diffusion methods. We view this as an engineering issue that can be mitigated through model compression techniques such as distillation, pruning, and consistency-model-based acceleration. In future work, we will investigate these strategies to reduce sampling steps and parameter count while preserving reconstruction quality, thereby enhancing UniE2F’s applicability in resource-constrained scenarios.

## Data Availability

All data used in our paper are publicly available. The details of the datasets and their acquisition are provided in Section 5.1 and Appendix B. Specifically, our synthetic data were generated using the DVS-Voltmeter [61] simulator based on the publicly accessible TrackingNet [60] dataset.

## Conflict of Interest

The authors affirm that there are no commercial or associative relationships that could be perceived as a conflict of interest related to the submitted work.

## References

- [1] Brandli, C., Berner, R., Yang, M., Liu, S.-C., Delbruck, T.: A  $240 \times 180$  130 db  $3 \mu\text{s}$  latency global shutter spatiotemporal vision sensor. *IEEE Journal of Solid-State Circuits* **49**(10), 2333–2341 (2014)
- [2] Brandli, C., Muller, L., Delbruck, T.: Real-time, high-speed video decompression using a frame- and event-based davis sensor. In: 2014 IEEE International Symposium on Circuits and Systems (ISCAS), pp. 686–689 (2014). IEEE
- [3] Wan, Z., Dai, Y., Mao, Y.: Learning dense and continuous optical flow from an event camera. *IEEE Transactions on Image Processing* **31**, 7237–7251 (2022)
- [4] Zhang, H., Zhang, L., Dai, Y., Li, H., Koniusz, P.: Event-guided multi-patch network with self-supervision for non-uniform motion deblurring. *International Journal of Computer Vision* **131**(2), 453–470 (2023)
- [5] Zhu, Z., Hou, J., Lyu, X.: Learning graph-embedded key-event back-tracing for object tracking in event clouds. *Advances in Neural Information Processing Systems* **35**, 7462–7476 (2022)
- [6] Zhu, Z., Hou, J., Wu, D.O.: Cross-modal orthogonal high-rank augmentation for rgb-event transformer-trackers. In: Proceedings of the IEEE/CVF International Conference on Computer Vision, pp. 22045–22055 (2023)
- [7] Chen, Z., Zhu, Z., Zhang, Y., Hou, J., Shi, G., Wu, J.: Segment any event streams via weighted adaptation of pivotal tokens. In: Proceedings of the IEEE/CVF Conference on Computer Vision and Pattern Recognition, pp. 3890–3900 (2024)

- [8] Zhu, Z., Hou, J., Li, J., Wu, J., Hou, J.: Modeling state shifting via local-global distillation for event-frame gaze tracking. *IEEE Transactions on Mobile Computing* (2025)
- [9] Rebecq, H., Ranftl, R., Koltun, V., Scaramuzza, D.: High speed and high dynamic range video with an event camera. *IEEE transactions on pattern analysis and machine intelligence* **43**(6), 1964–1980 (2019)
- [10] Gallego, G., Delbrück, T., Orchard, G., Bartolozzi, C., Taba, B., Censi, A., Leutenegger, S., Davison, A.J., Conradt, J., Daniilidis, K., *et al.*: Event-based vision: A survey. *IEEE transactions on pattern analysis and machine intelligence* **44**(1), 154–180 (2020)
- [11] Stoffregen, T., Scheerlinck, C., Scaramuzza, D., Drummond, T., Barnes, N., Kleeman, L., Mahony, R.: Reducing the sim-to-real gap for event cameras. In: *Computer Vision—ECCV 2020: 16th European Conference, Glasgow, UK, August 23–28, 2020, Proceedings, Part XXVII 16*, pp. 534–549 (2020). Springer
- [12] Scheerlinck, C., Rebecq, H., Gehrig, D., Barnes, N., Mahony, R., Scaramuzza, D.: Fast image reconstruction with an event camera. In: *Proceedings of the IEEE/CVF Winter Conference on Applications of Computer Vision*, pp. 156–163 (2020)
- [13] Cadena, P.R.G., Qian, Y., Wang, C., Yang, M.: Spade-e2vid: Spatially-adaptive denormalization for event-based video reconstruction. *IEEE Transactions on Image Processing* **30**, 2488–2500 (2021)
- [14] Weng, W., Zhang, Y., Xiong, Z.: Event-based video reconstruction using transformer. In: *Proceedings of the IEEE/CVF International Conference on Computer Vision*, pp. 2563–2572 (2021)
- [15] Dong, J., Ota, K., Dong, M.: Video frame interpolation: A comprehensive survey. *ACM Transactions on Multimedia Computing, Communications and Applications* **19**(2s), 1–31 (2023)
- [16] Li, S., Fang, J., Xu, H., Xue, J.: Video frame prediction by deep multi-branch mask network. *IEEE Transactions on Circuits and Systems for Video Technology* **31**(4), 1283–1295 (2020)
- [17] Tulyakov, S., Gehrig, D., Georgoulis, S., Erbach, J., Gehrig, M., Li, Y., Scaramuzza, D.: Time lens: Event-based video frame interpolation. In: *Proceedings of the IEEE/CVF Conference on Computer Vision and Pattern Recognition*, pp. 16155–16164 (2021)
- [18] Tulyakov, S., Bochicchio, A., Gehrig, D., Georgoulis, S., Li, Y., Scaramuzza, D.: Time Lens++: Event-based frame interpolation with non-linear parametric flow and multi-scale fusion. *IEEE Conference on Computer Vision and Pattern Recognition* (2022)
- [19] Zhu, J., Wan, Z., Dai, Y.: Video frame prediction from a single image and events. In: *AAAI Conference on Artificial Intelligence (AAAI)* (2024)
- [20] Wang, Z., Hamann, F., Chaney, K., Jiang, W., Gallego, G., Daniilidis, K.: Event-based continuous color video decompression from single frames. In: *Proceedings of the Computer Vision and Pattern Recognition Conference*, pp. 4968–4978 (2025)
- [21] Ho, J., Jain, A., Abbeel, P.: Denoising diffusion probabilistic models. *Advances in neural information processing systems* **33**, 6840–6851 (2020)
- [22] Kawar, B., Elad, M., Ermon, S., Song, J.: Denoising diffusion restoration models. *Advances in Neural Information Processing Systems* **35**, 23593–23606 (2022)
- [23] Chung, H., Kim, J., Mccann, M.T., Klasky, M.L., Ye, J.C.: Diffusion posterior sampling for general noisy inverse problems. In: *The Eleventh International Conference on Learning Representations* (2023)
- [24] Wang, Y., Yu, J., Zhang, J.: Zero-shot image restoration using denoising diffusion null-space model. In: *The Eleventh International Conference on Learning Representations* (2023)

- [25] Saharia, C., Ho, J., Chan, W., Salimans, T., Fleet, D.J., Norouzi, M.: Image super-resolution via iterative refinement. *IEEE transactions on pattern analysis and machine intelligence* **45**(4), 4713–4726 (2022)
- [26] Saharia, C., Chan, W., Chang, H., Lee, C., Ho, J., Salimans, T., Fleet, D., Norouzi, M.: Palette: Image-to-image diffusion models. In: *ACM SIGGRAPH 2022 Conference Proceedings*, pp. 1–10 (2022)
- [27] Gao, S., Liu, X., Zeng, B., Xu, S., Li, Y., Luo, X., Liu, J., Zhen, X., Zhang, B.: Implicit diffusion models for continuous super-resolution. In: *Proceedings of the IEEE/CVF Conference on Computer Vision and Pattern Recognition*, pp. 10021–10030 (2023)
- [28] Rombach, R., Blattmann, A., Lorenz, D., Esser, P., Ommer, B.: High-resolution image synthesis with latent diffusion models. In: *Proceedings of the IEEE/CVF Conference on Computer Vision and Pattern Recognition*, pp. 10684–10695 (2022)
- [29] Blattmann, A., Dockhorn, T., Kulal, S., Mendelevitch, D., Kilian, M., Lorenz, D., Levi, Y., English, Z., Voleti, V., Letts, A., et al.: Stable video diffusion: Scaling latent video diffusion models to large datasets. *arXiv preprint arXiv:2311.15127* (2023)
- [30] Tulyakov, S., Boicchio, A., Gehrig, D., Georgoulis, S., Li, Y., Scaramuzza, D.: Time lens++: Event-based frame interpolation with parametric non-linear flow and multi-scale fusion. In: *Proceedings of the IEEE/CVF Conference on Computer Vision and Pattern Recognition*, pp. 17755–17764 (2022)
- [31] He, W., You, K., Qiao, Z., Jia, X., Zhang, Z., Wang, W., Lu, H., Wang, Y., Liao, J.: Timereplayer: Unlocking the potential of event cameras for video interpolation. In: *Proceedings of the IEEE/CVF Conference on Computer Vision and Pattern Recognition*, pp. 17804–17813 (2022)
- [32] Wu, S., You, K., He, W., Yang, C., Tian, Y., Wang, Y., Zhang, Z., Liao, J.: Video interpolation by event-driven anisotropic adjustment of optical flow. In: *European Conference on Computer Vision*, pp. 267–283 (2022). Springer
- [33] Pan, L., Scheerlinck, C., Yu, X., Hartley, R., Liu, M., Dai, Y.: Bringing a blurry frame alive at high frame-rate with an event camera. In: *Proceedings of the IEEE/CVF Conference on Computer Vision and Pattern Recognition*, pp. 6820–6829 (2019)
- [34] Pan, L., Hartley, R., Scheerlinck, C., Liu, M., Yu, X., Dai, Y.: High frame rate video reconstruction based on an event camera. *IEEE Transactions on Pattern Analysis and Machine Intelligence* **44**(5), 2519–2533 (2020)
- [35] Chen, Z., Wu, J., Hou, J., Li, L., Dong, W., Shi, G.: Ecsnet: Spatio-temporal feature learning for event camera. *IEEE Transactions on Circuits and Systems for Video Technology* **33**(2), 701–712 (2022)
- [36] Cook, M., Gugelmann, L., Jug, F., Krautz, C., Steger, A.: Interacting maps for fast visual interpretation. In: *The 2011 International Joint Conference on Neural Networks*, pp. 770–776 (2011). IEEE
- [37] Kim, H., Handa, A., Benosman, R., Ieng, S.-H., Davison, A.J.: Simultaneous mosaicing and tracking with an event camera. *J. Solid State Circ* **43**, 566–576 (2008)
- [38] Munda, G., Reinbacher, C., Pock, T.: Real-time intensity-image reconstruction for event cameras using manifold regularisation. *International Journal of Computer Vision* **126**(12), 1381–1393 (2018)
- [39] Bardow, P., Davison, A.J., Leutenegger, S.: Simultaneous optical flow and intensity estimation from an event camera. In: *Proceedings of the IEEE Conference on Computer Vision and Pattern Recognition*, pp. 884–892 (2016)
- [40] Paredes-Vallés, F., De Croon, G.C.: Back to event basics: Self-supervised learning of

- image reconstruction for event cameras via photometric constancy. In: Proceedings of the IEEE/CVF Conference on Computer Vision and Pattern Recognition, pp. 3446–3455 (2021)
- [41] Liang, Q., Zheng, X., Huang, K., Zhang, Y., Chen, J., Tian, Y.: Event-diffusion: Event-based image reconstruction and restoration with diffusion models. In: Proceedings of the 31st ACM International Conference on Multimedia, pp. 3837–3846 (2023)
- [42] Zhu, L., Zheng, Y., Zhang, Y., Wang, X., Wang, L., Huang, H.: Temporal residual guided diffusion framework for event-driven video reconstruction. In: Computer Vision – ECCV 2024: 18th European Conference, Milan, Italy, September 29–October 4, 2024, Proceedings, Part XL, pp. 411–427. Springer, Cham, Switzerland (2024)
- [43] Chen, K., Li, H., Zhou, J., Wang, Z., Wang, L.: Lase-e2v: Towards language-guided semantic-aware event-to-video reconstruction. *Advances in Neural Information Processing Systems* **37**, 70406–70430 (2024)
- [44] Liang, J., Yu, B., Yang, Y., Han, Y., Shi, B.: E2vidiff: Perceptual events-to-video reconstruction using diffusion priors. arXiv preprint arXiv:2407.08231 (2024)
- [45] Zhao, Y., Zhang, P., Wang, C., Lam, E.Y.: Controllable unsupervised event-based video generation. In: 2024 IEEE International Conference on Image Processing (ICIP), pp. 2278–2284 (2024). IEEE
- [46] Tulyakov, S., Bochicchio, A., Gehrig, D., Georgoulis, S., Li, Y., Scaramuzza, D.: Time lens++: Event-based frame interpolation with parametric non-linear flow and multi-scale fusion. *IEEE Conference on Computer Vision and Pattern Recognition (CVPR)* (2022)
- [47] Liu, H., Xu, J., Chang, Y., Zhou, H., Zhao, H., Wang, L., Yan, L.: Timetracker: Event-based continuous point tracking for video frame interpolation with non-linear motion. In: Proceedings of the Computer Vision and Pattern Recognition Conference, pp. 17649–17659 (2025)
- [48] Ma, Y., Guo, S., Chen, Y., Xue, T., Gu, J.: Timelens-xl: Real-time event-based video frame interpolation with large motion. In: European Conference on Computer Vision, pp. 178–194 (2024). Springer
- [49] Kim, T., Chae, Y., Jang, H.-K., Yoon, K.-J.: Event-based video frame interpolation with cross-modal asymmetric bidirectional motion fields. In: Proceedings of the IEEE/CVF Conference on Computer Vision and Pattern Recognition, pp. 18032–18042 (2023)
- [50] Chen, J., Feng, B.Y., Cai, H., Wang, T., Burner, L., Yuan, D., Fermuller, C., Metzler, C.A., Aloimonos, Y.: Repurposing pre-trained video diffusion models for event-based video interpolation. In: Proceedings of the Computer Vision and Pattern Recognition Conference, pp. 12456–12466 (2025)
- [51] Xia, B., Zhang, Y., Wang, S., Wang, Y., Wu, X., Tian, Y., Yang, W., Van Gool, L.: Diffir: Efficient diffusion model for image restoration. In: Proceedings of the IEEE/CVF International Conference on Computer Vision, pp. 13095–13105 (2023)
- [52] Blattmann, A., Rombach, R., Ling, H., Dockhorn, T., Kim, S.W., Fidler, S., Kreis, K.: Align your latents: High-resolution video synthesis with latent diffusion models. In: Proceedings of the IEEE/CVF Conference on Computer Vision and Pattern Recognition, pp. 22563–22575 (2023)
- [53] Wang, L., Ho, Y.-S., Yoon, K.-J., *et al.*: Event-based high dynamic range image and very high frame rate video generation using conditional generative adversarial networks. In: Proceedings of the IEEE/CVF Conference on Computer Vision and Pattern Recognition, pp. 10081–10090 (2019)
- [54] Nam, Y., Mostafavi, M., Yoon, K.-J., Choi, J.: Stereo depth from events cameras: Concentrate and focus on the future. In: Proceedings of the IEEE/CVF Conference on Computer Vision and Pattern Recognition,

- pp. 6114–6123 (2022)
- [55] Teng, M., Zhou, C., Lou, H., Shi, B.: Nest: Neural event stack for event-based image enhancement. In: European Conference on Computer Vision, pp. 660–676 (2022). Springer
- [56] Song, Y., Sohl-Dickstein, J., Kingma, D.P., Kumar, A., Ermon, S., Poole, B.: Score-based generative modeling through stochastic differential equations. In: International Conference on Learning Representations (2021)
- [57] Wu, S., Zhu, Z., Hou, J., Shi, G., Wu, J.: E-motion: Future motion simulation via event sequence diffusion. *Advances in Neural Information Processing Systems* **37**, 105552–105582 (2024)
- [58] Karras, T., Aittala, M., Aila, T., Laine, S.: Elucidating the design space of diffusion-based generative models. *Advances in neural information processing systems* **35**, 26565–26577 (2022)
- [59] He, K., Zhang, X., Ren, S., Sun, J.: Deep residual learning for image recognition. In: Proceedings of the IEEE Conference on Computer Vision and Pattern Recognition, pp. 770–778 (2016)
- [60] Muller, M., Bibi, A., Giancola, S., Alsubaihi, S., Ghanem, B.: Trackingnet: A large-scale dataset and benchmark for object tracking in the wild. In: Proceedings of the European Conference on Computer Vision (ECCV), pp. 300–317 (2018)
- [61] Lin, S., Ma, Y., Guo, Z., Wen, B.: Dvs-voltmeter: Stochastic process-based event simulator for dynamic vision sensors. In: European Conference on Computer Vision, pp. 578–593 (2022). Springer
- [62] Ercan, B., Eker, O., Saglam, C., Erdem, A., Erdem, E.: Hypere2vid: Improving event-based video reconstruction via hypernetworks. *IEEE Transactions on Image Processing* **33**, 1826–1837 (2024)
- [63] Loshchilov, I., Hutter, F.: Decoupled weight decay regularization. In: International Conference on Learning Representations (2019)
- [64] Wang, Z., Bovik, A.C., Sheikh, H.R., Simoncelli, E.P.: Image quality assessment: from error visibility to structural similarity. *IEEE transactions on image processing* **13**(4), 600–612 (2004)
- [65] Zhang, R., Isola, P., Efros, A.A., Shechtman, E., Wang, O.: The unreasonable effectiveness of deep features as a perceptual metric. In: Proceedings of the IEEE Conference on Computer Vision and Pattern Recognition, pp. 586–595 (2018)
- [66] Zhu, J., Wan, Z., Dai, Y.: Video frame prediction from a single image and events. In: AAAI Conference on Artificial Intelligence (AAAI) (2024)
- [67] Mueggler, E., Rebecq, H., Gallego, G., Delbruck, T., Scaramuzza, D.: The event-camera dataset and simulator: Event-based data for pose estimation, visual odometry, and slam. *The International journal of robotics research* **36**(2), 142–149 (2017)
- [68] Zhu, A.Z., Thakur, D., Özaslan, T., Pfrommer, B., Kumar, V., Daniilidis, K.: The multivehicle stereo event camera dataset: An event camera dataset for 3d perception. *IEEE Robotics and Automation Letters* **3**(3), 2032–2039 (2018)
- [69] Heusel, M., Ramsauer, H., Unterthiner, T., Nessler, B., Hochreiter, S.: Gans trained by a two time-scale update rule converge to a local nash equilibrium. *Advances in neural information processing systems* **30** (2017)
- [70] Lin, T.-Y., Maire, M., Belongie, S., Hays, J., Perona, P., Ramanan, D., Dollár, P., Zitnick, C.L.: Microsoft coco: Common objects in context. In: Computer vision–ECCV 2014: 13th European Conference, Zurich, Switzerland, September 6–12, 2014, Proceedings, Part V 13, pp. 740–755 (2014). Springer

# Appendix Contents

- [A Proofs of Proposition 1](#)
- [B Details of Datasets](#)
- [C Training Strategy for the Inter-Frame Residual Estimator](#)
- [D More Visual Results](#)
- [E Detailed Experiment Settings for Video Frame Interpolation and Prediction](#)

## Appendix A Proofs of Proposition 1

### A.1 Gradient Alignment with the Tangent Space & Manifold-preserved Sampling

Proof of **Gradient Alignment with the Tangent Space** is based on the following **assumptions**:

- the data manifold  $\mathcal{M}$  is a smooth embedded submanifold of  $\mathbb{R}^n$ ;
- the decoder  $\mathcal{D} : \mathcal{M} \rightarrow \mathcal{P}$  (pixel space) is differentiable with a full-rank Jacobian  $J_{\mathcal{D}}$ , corresponding to the state  $\mathbf{U}^t$ .

Due to that our introduced residual loss is defined in pixel space as

$$\mathcal{L}_{\text{residual}} = \|\Delta\mathcal{D}(\mathbf{U}^t) - \mathbf{R}\|_1, \quad (\text{A1})$$

where  $\Delta\mathcal{D}(\mathbf{U}^t) = \mathcal{D}(\mathbf{U}_{1:F}^t) - \mathcal{D}(\mathbf{U}_{0:F-1}^t)$ . Then, the gradient in pixel space is:

$$\nabla_{\Delta\mathbf{F}}\mathcal{L}_{\text{residual}} = \text{sign}(\Delta\mathbf{F} - \mathbf{R}). \quad (\text{A2})$$

By the chain rule, the gradient in latent space is:

$$\nabla_{\mathbf{U}^t}\mathcal{L}_{\text{residual}} = J_{\mathcal{D}}^{\top}(\mathbf{U}^t) \cdot \nabla_{\Delta\mathbf{F}}\mathcal{L}_{\text{residual}}, \quad (\text{A3})$$

where  $J_{\mathcal{D}}$  is the Jacobian of  $\mathcal{D}$ . Since  $\mathcal{D}$  maps  $\mathcal{M}$  to  $\mathcal{P}$ ,  $J_{\mathcal{D}}$  acts as a linear map from  $T_{\mathbf{U}^t}\mathcal{M}$  to  $T_{\mathcal{D}(\mathbf{U}^t)}\mathcal{P}$ . Thus,  $\nabla_{\mathbf{U}^t}\mathcal{L}_{\text{residual}} \in T_{\mathbf{U}^t}\mathcal{M}$ .

Then, we prove that our proposed updating is **manifold-preserved**. The part is based on the following assumption: The step size  $s$  satisfies  $s \cdot \|\nabla_{\mathbf{U}^t}\mathcal{L}_{\text{residual}}\| < \delta$ , where  $\delta$  is the injectivity radius of  $\mathcal{M}$  at  $\mathbf{U}^t$ .

The exponential map  $\exp_{\mathbf{U}^t} : T_{\mathbf{U}^t}\mathcal{M} \rightarrow \mathcal{M}$  defines a local diffeomorphism (a mapping

between a group of manifolds with similar structure) [23] within the radius  $\delta$ . Then, we can express the update via the exponential map:

$$\tilde{\mathbf{U}}^t = \exp_{\mathbf{U}^t}(-s\nabla_{\mathbf{U}^t}\mathcal{L}_{\text{residual}}). \quad (\text{A4})$$

For  $s \cdot \|\nabla_{\mathbf{U}^t}\mathcal{L}_{\text{residual}}\| < \delta$ ,  $\exp_{\mathbf{U}^t}$  ensures  $\tilde{\mathbf{U}}^t \in \mathcal{M}$ . Thus, for small  $s$ , the update approximates the Euclidean step:

$$\tilde{\mathbf{U}}^t \approx \mathbf{U}^t - s\nabla_{\mathbf{U}^t}\mathcal{L}_{\text{residual}} + \mathcal{O}(s^2\|\nabla_{\mathbf{U}^t}\mathcal{L}_{\text{residual}}\|^2), \quad (\text{A5})$$

with higher-order terms bounded by the sectional curvature of  $\mathcal{M}$ . Due to that we have proved that our updating gradient is in the tangent space of diffusion manifold, thus, .

### A.2 Reconstruction Error is Bounded

We first reclaim the following **notions**. Let  $\mathbf{V} = \{\mathbf{V}_0, \mathbf{V}_1, \dots, \mathbf{V}_{F-1}\}$  denote the ground truth video frames. Let  $\mathbf{F} = \{\mathbf{F}_0, \mathbf{F}_1, \dots, \mathbf{F}_{F-1}\}$  denote the reconstructed frames, where  $\mathbf{F}_k = \mathcal{D}(\mathbf{U}_k)$ . Moreover, we also claim the following assumptions, which is the base for the following proof.

- The event-derived residual  $\mathbf{R}_k$  approximates  $C \cdot \Delta\mathbf{V}_k$ , where  $C$  is the event camera’s contrast threshold, and  $\Delta\mathbf{V}_k = \mathbf{V}_{k+1} - \mathbf{V}_k$ .
- The decoder  $\mathcal{D} : \mathcal{M} \rightarrow \mathcal{P}$  is  $L$ -Lipschitz smooth, i.e.,  $\|\mathcal{D}(\mathbf{U}) - \mathcal{D}(\mathbf{U}')\| \leq L\|\mathbf{U} - \mathbf{U}'\|$ .
- The Jacobian  $J_{\mathcal{D}}$  of  $\mathcal{D}$  is full-rank and bounded:  $\|J_{\mathcal{D}}\| \leq L$ ,  $\|J_{\mathcal{D}}^{-1}\| \leq \kappa$ , where  $\kappa$  is the condition number.

Note that we have the following residual loss to train the encoder. It enforces alignment between reconstructed and event-derived residuals:

$$\mathcal{L}_{\text{residual}} = \sum_{k=0}^{F-2} \|\Delta\mathbf{F}_k - \mathbf{R}_k\|_1, \quad (\text{A6})$$

where  $\Delta\mathbf{F}_k = \mathbf{F}_{k+1} - \mathbf{F}_k$ . From the event camera model:

$$\mathbf{R}_k = C \cdot \Delta\mathbf{V}_k + \boldsymbol{\epsilon}_k, \quad \|\boldsymbol{\epsilon}_k\|_1 \leq \varepsilon, \quad (\text{A7})$$

where  $\boldsymbol{\epsilon}_k$  captures event noise and threshold approximation errors.

We first to find the correlation with the residual loss and frame reconstruction error. The reconstruction error for frame  $k$  is:

$$\|\mathbf{F}_k - \mathbf{V}_k\|_1 \leq \sum_{i=0}^{k-1} \|\Delta \mathbf{F}_i - \Delta \mathbf{V}_i\|_1. \quad (\text{A8})$$

By using the triangle inequality, we have

$$\|\Delta \mathbf{F}_i - \Delta \mathbf{V}_i\|_1 \leq \|\Delta \mathbf{F}_i - \mathbf{R}_i/C\|_1 + \|\mathbf{R}_i/C - \Delta \mathbf{V}_i\|_1. \quad (\text{A9})$$

Then, through substituting  $\mathbf{R}_k = C \cdot \Delta \mathbf{V}_k + \epsilon_k$  into aforementioned equation, we have

$$\|\Delta \mathbf{F}_i - \Delta \mathbf{V}_i\|_1 \leq \frac{1}{C} \|\Delta \mathbf{F}_i - \mathbf{R}_i\|_1 + \frac{1}{C} \|\epsilon_i\|_1. \quad (\text{A10})$$

Summing over all frames:

$$\|\mathbf{F}_k - \mathbf{V}_k\|_1 \leq \frac{1}{C} \sum_{i=0}^{k-1} (\|\Delta \mathbf{F}_i - \mathbf{R}_i\|_1 + \epsilon). \quad (\text{A11})$$

Then, we try to bound the latent space deviation. The residual loss gradient corrects the latent  $\mathbf{U}$  via:

$$\tilde{\mathbf{U}}_k = \mathbf{U}_k - s \nabla_{\mathbf{U}_k} \mathcal{L}_{\text{residual}}. \quad (\text{A12})$$

Using the Lipschitz continuity of  $\mathcal{D}$ :

$$\|\Delta \mathbf{F}_k - \mathbf{R}_k\|_1 \leq L \|\Delta \mathbf{U}_k - \Delta \mathbf{U}_k^*\|_1, \quad (\text{A13})$$

where  $\Delta \mathbf{U}_k^* = J_{\mathcal{D}}^{-1} \cdot \Delta \mathbf{V}_k$  is the ideal latent residual. From the Jacobian bound:

$$\|\Delta \mathbf{U}_k - \Delta \mathbf{U}_k^*\|_1 \leq \kappa \|\Delta \mathbf{F}_k - C \cdot \Delta \mathbf{V}_k\|_1. \quad (\text{A14})$$

**Final Reconstruction Error Bound.** Combining the above:

$$\|\mathbf{F} - \mathbf{V}\|_1 \leq \frac{1}{C} \sum_{k=0}^{F-2} (L \cdot \kappa \|\Delta \mathbf{F}_k - C \cdot \Delta \mathbf{V}_k\|_1 + \epsilon). \quad (\text{A15})$$

Substituting  $\|\Delta \mathbf{F}_k - C \cdot \Delta \mathbf{V}_k\|_1 \leq \|\Delta \mathbf{F}_k - \mathbf{R}_k\|_1 + \|\mathbf{R}_k - C \cdot \Delta \mathbf{V}_k\|_1$ : Then, we can draw the final conclusion that the total reconstruction error is bounded by:

$$\|\mathbf{F} - \mathbf{V}\|_1 \leq \underbrace{\frac{L\kappa}{C} \mathcal{L}_{\text{residual}}}_{\text{Controlled by gradient guidance}} + \underbrace{\frac{F\epsilon}{C}}_{\text{Event model error}}. \quad (\text{A16})$$

Minimizing  $\mathcal{L}_{\text{residual}}$  directly reduces the error, while the term  $\frac{F\epsilon}{C}$  is inherent to event data noise.

## Appendix B Details of Datasets

The training of the network relies on a sufficiently large collection of event sequences paired with corresponding ground-truth video frames. However, due to the limited availability of real-world datasets, we employ the event simulator to synthesize a large-scale training dataset from existing video data. Specifically, we select 1,800 video frame sequences which have large motion from TrackingNet [60]—a large-scale object tracking dataset that has an extensive collection of real-world scenarios captured from YouTube videos. Each sequence comprises approximately 400 to 500 frames. Subsequently, we employ the DVS-Voltmeter [61] to simulate event streams between consecutive frames, thereby creating synthetic event data. Unlike previous works that generate synthetic datasets from MS-COCO [70], which only contains globally homographic motion, our dataset is simulated from real-world videos and incorporates both globally homomorphic motion and locally independent motion. This diversity can enable the network to generalize effectively to the various camera movements and scene variations encountered in real-world scenarios.

To ensure an accurate assessment of the algorithm’s performance in reconstructing video frames, we also construct a synthetic test set and a real-world test set. The synthetic test set is created by selecting 212 video frame sequences from TrackingNet [60], with each sequence containing 12 frames. In contrast, the real-world test set, consisting of video sequences (each with 12 frames), is collected from the High-Speed Events and RGB

(HS-ERGB) [17] dataset, which contains synchronized event data and RGB frames recorded from a hybrid camera system.

## Appendix C Training Strategy for the Inter-Frame Residual Estimator

First, we select event streams and their corresponding RGB video frames from the synthetic dataset’s training set, and convert each event stream into a three-channel event representation; then, this representation is fed into a ResNet backbone (identical to the standard ResNet except that its output layer is modified to predict pixel-level residuals between consecutive frames). During training, we supervise the network with the pixel-wise difference between consecutive video frames,  $\mathbf{V}_{t+1} - \mathbf{V}_t$ , and optimize it by minimizing the  $L_1$  loss between the predicted and ground-truth residuals. The network is trained for 9,000 iterations with the Adam optimizer ( $\beta_1 = 0.9$ ,  $\beta_2 = 0.999$ ) at a fixed learning rate of  $1 \times 10^{-4}$ . This setup ensures the estimator effectively learns the mapping from event representations to inter-frame residuals, providing accurate priors for the subsequent residual guidance.

## Appendix D More Visual Results

From Figure D1 to Figure D8, we provide additional visual comparisons to demonstrate that our method achieves superior performance.

## Appendix E Detailed Experiment Settings for Video Frame Interpolation and Prediction

Given a sequence of twelve consecutive frames from the test set, the network takes the reference

frames in the case of video frame interpolation (VFI) to reconstruct the intermediate frames, or the first frame in the case of video frame prediction (VFP) to generate the subsequent frames.

For the interpolation task, to ensure compatibility with different interpolation factors supported by various pretrained baselines, we introduce two temporal up-sampling settings during evaluation: VFI-4 $\times$  and VFI-11 $\times$ . Specifically, in the VFI-4 $\times$  setting, we use frames at indices 0, 4, 8 as references and interpolate six intermediate frames (three intermediate frames between each pair. i.e., frames 1–3 for 0, 4 and 5–7 for 4, 8). In the VFI-11 $\times$  setting, we interpolate ten frames between frames at indices 0, 11. For the prediction task, we use the first frame at index 0 to generate the subsequent eleven frames at indices from 1 to 11. After obtaining the intermediate or subsequent frames from the network output, we compare them with the corresponding ground-truth frames from the test set to compute MSE, SSIM, and LPIPS.

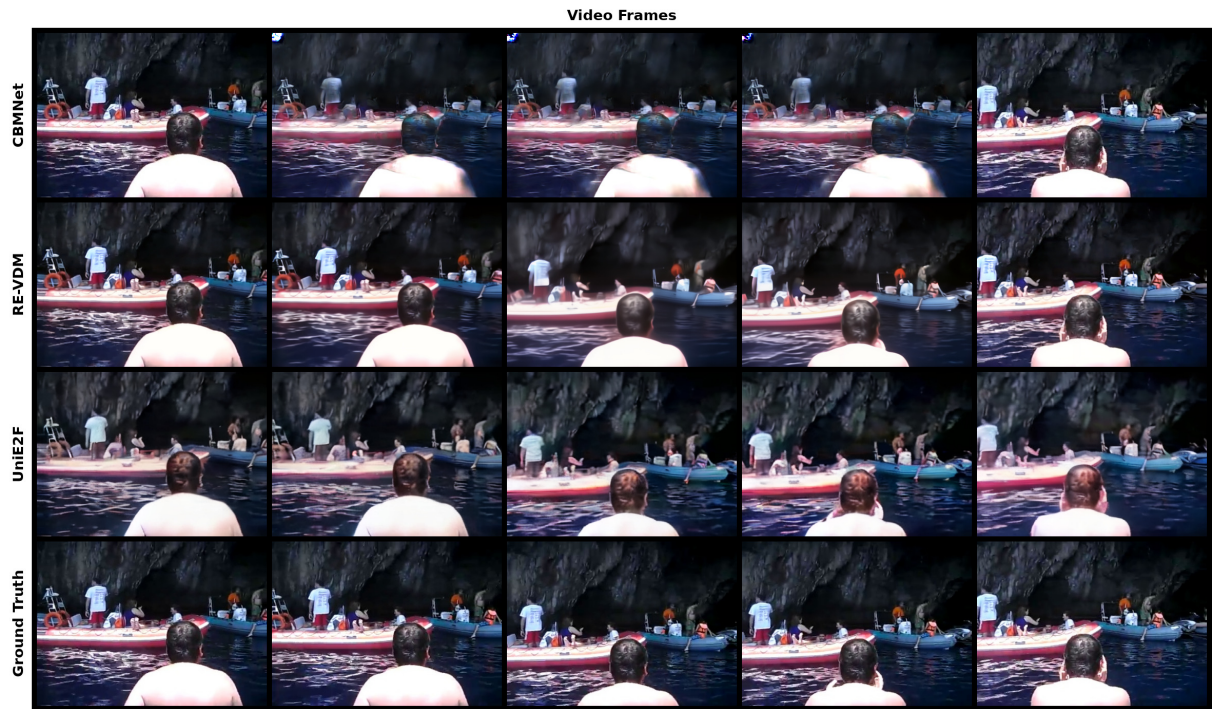


Fig. D1: Visual comparison of event-based video frame Interpolation results on synthetic dataset.

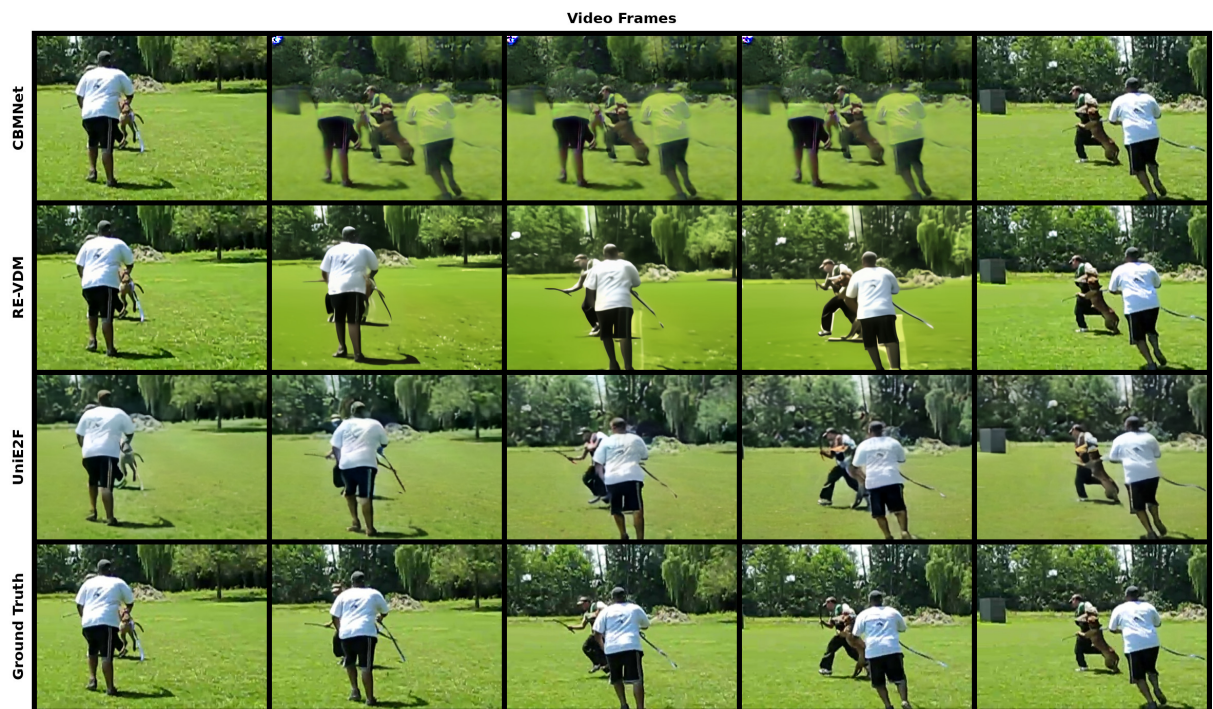


Fig. D2: Visual comparison of event-based video frame Interpolation results on synthetic dataset.



Fig. D3: Visual comparison of event-based video frame Interpolation results on synthetic dataset.

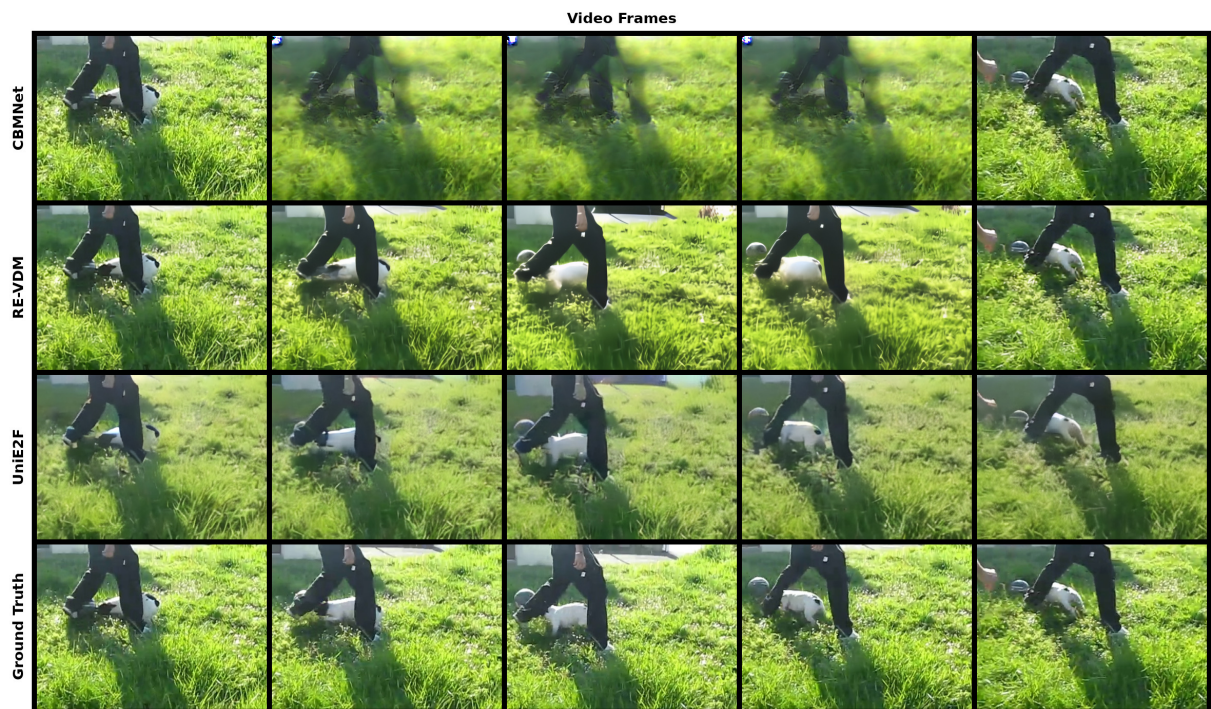
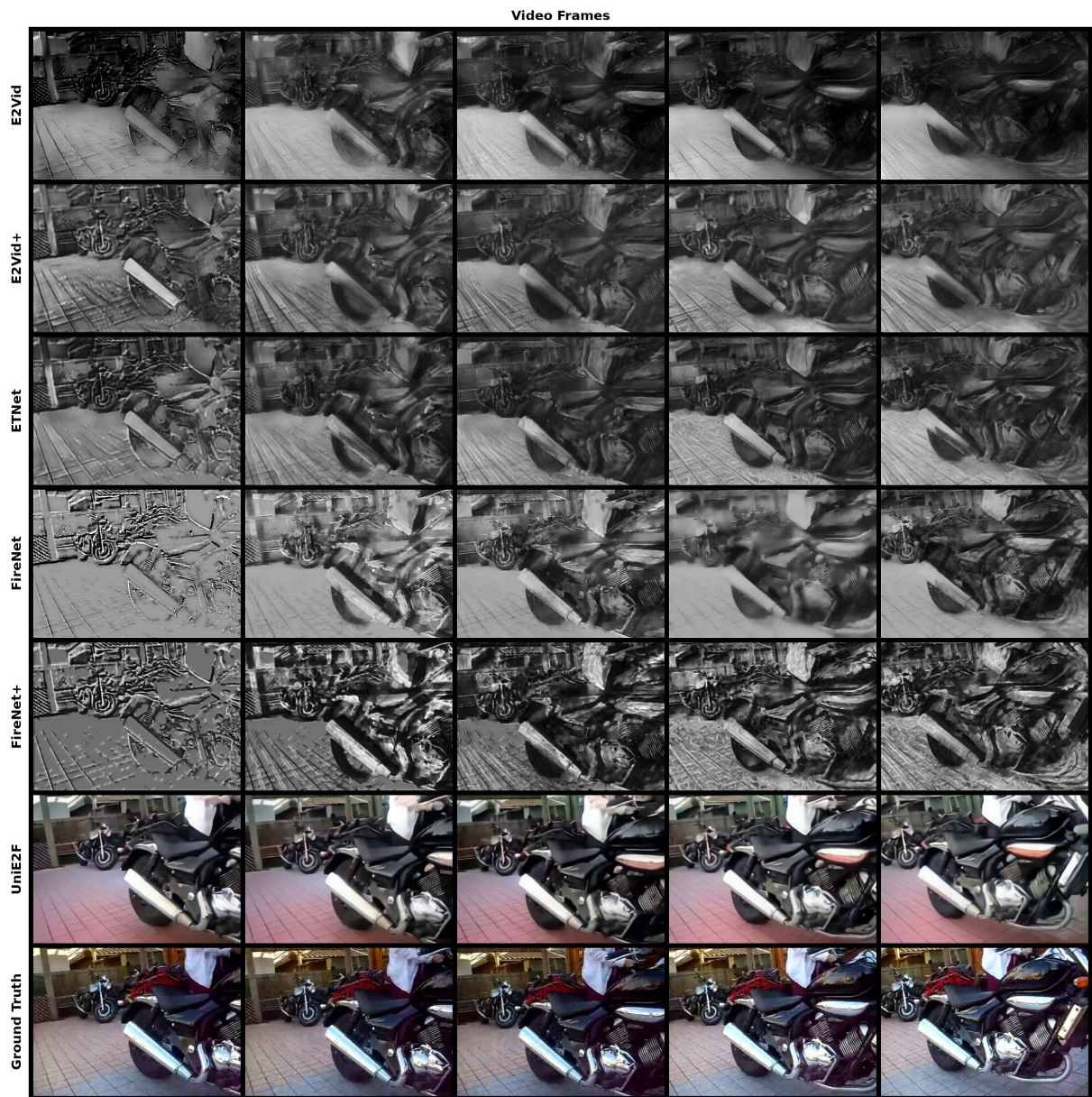


Fig. D4: Visual comparison of event-based video frame Interpolation results on synthetic dataset.



Fig. D5: Visual comparison of event-based video frame reconstruction results on synthetic dataset.



**Fig. D6:** Visual comparison of event-based video frame reconstruction results on synthetic dataset.

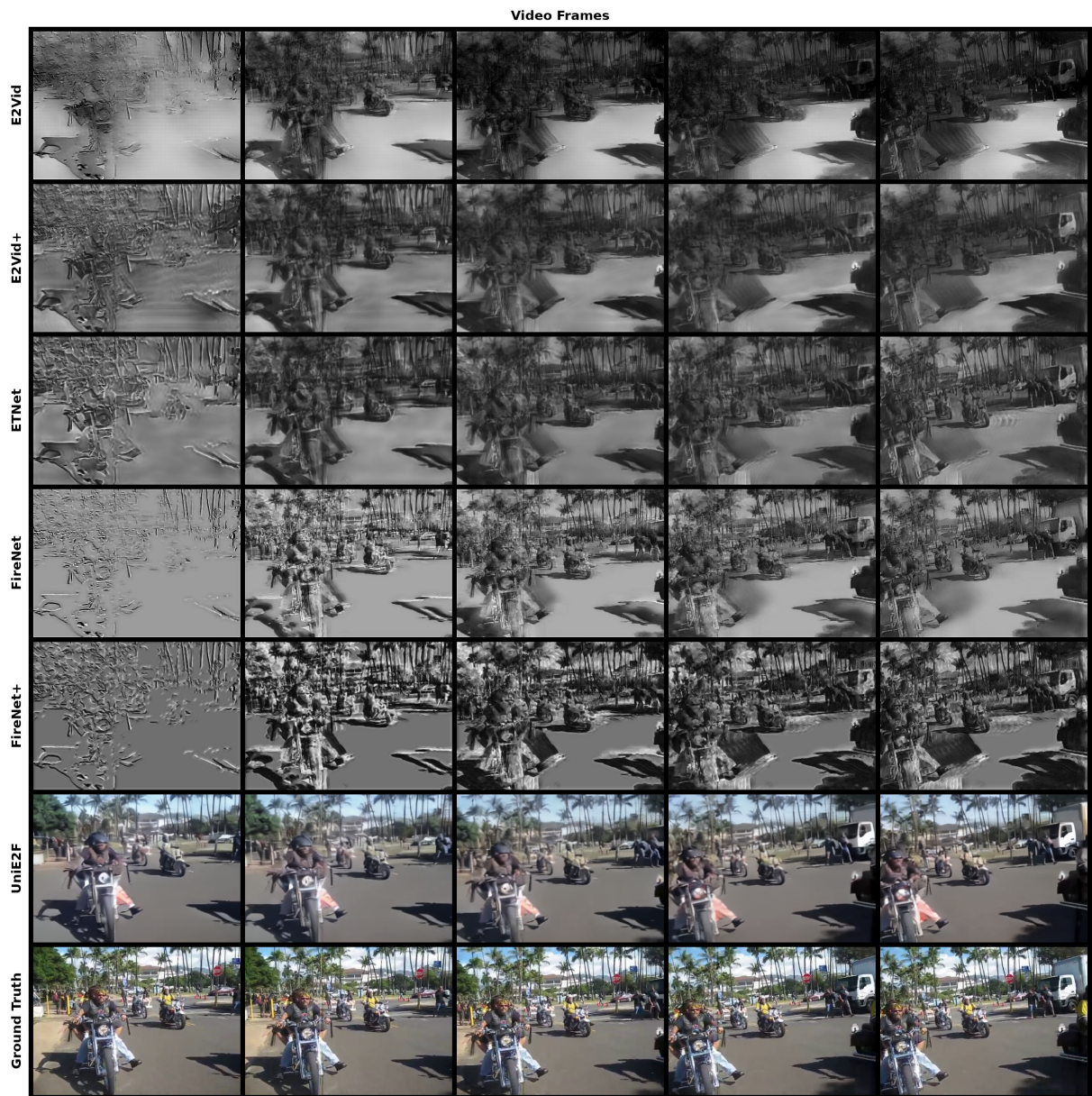


Fig. D7: Visual comparison of event-based video frame reconstruction results on synthetic dataset.

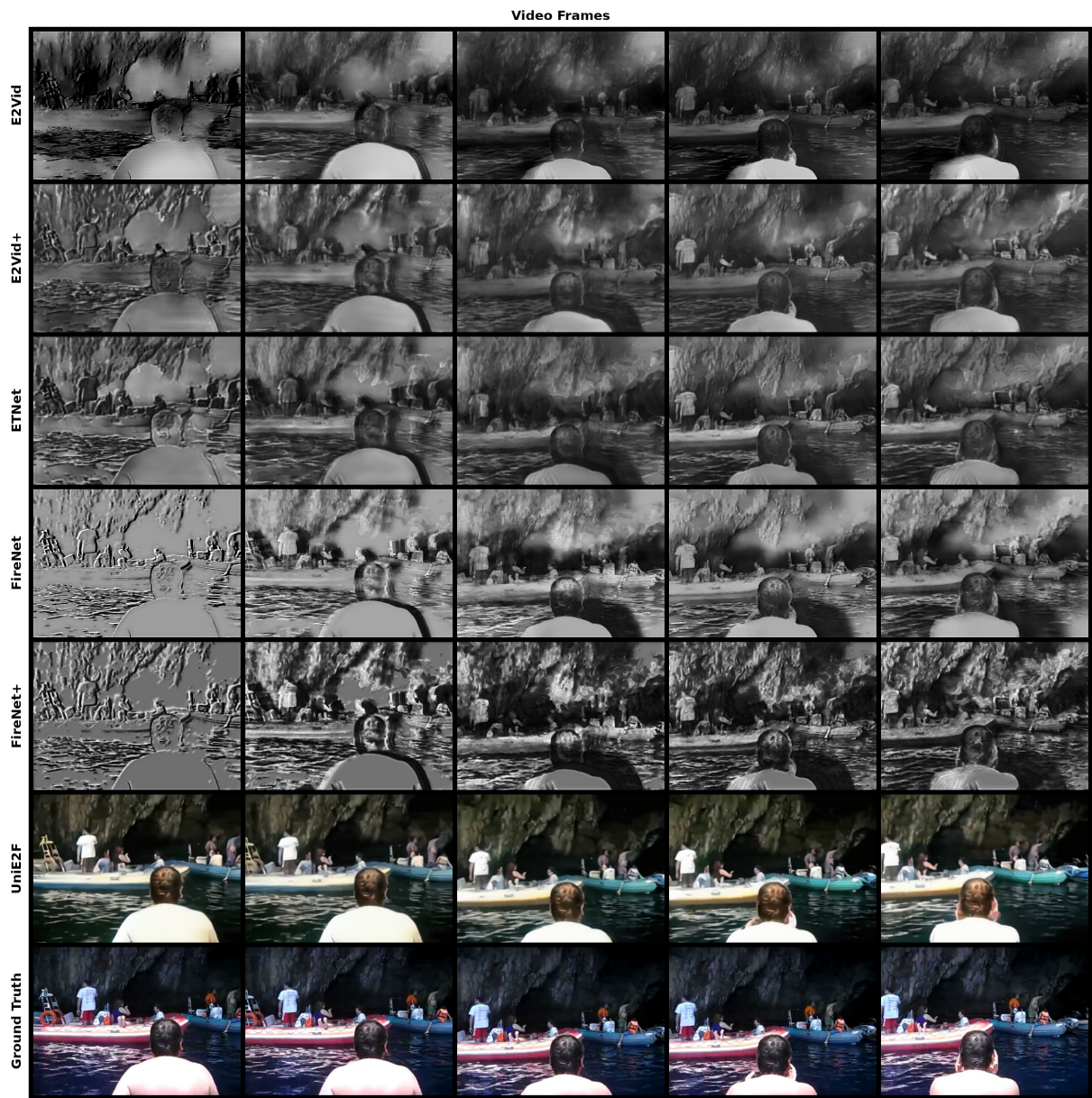


Fig. D8: Visual comparison of event-based video frame reconstruction results on synthetic dataset.